In Situ NMR Metrology Reveals Reaction Mechanisms in Flow Batteries

Evan Wenbo Zhao,[1] Tao Liu,[1#] Erlendur Jónsson,[1,2] Jeongjae Lee,[1] Israel Temprano,[1]
Rajesh B. Jethwa,[1] Anqi Wang,[3] Holly Smith,[1] Javier Carretero González,[4] Qilei Song,[3]
Clare P. Grey[1]*

[1]Department of Chemistry, Lensfield Road, University of Cambridge, Cambridge CB2 1EW, UK.
[2]Department of Physics, Chalmers University of Technology, Gothenburg SE 412 96, Sweden
[3]Barrer Centre, Department of Chemical Engineering, Imperial College London, London SW7 2AZ,
UK.
[4]Institute of Polymer Science and Technology, ICTP-CSIC, C/ Juan de la Cierva, nº 3, 28006,
Madrid, Spain.
*Correspondence to: cpg27@cam.ac.uk
present address: Shanghai Key Laboratory of Chemical Assessment and Sustainability, Department
of Chemistry, Tongji University, Shanghai 200092, P. R. China.

**Large-scale energy storage is becoming increasingly critical to balance the intermittency
between renewable energy production and consumption[1]. Organic redox flow batteries (RFBs),
based on inexpensive and sustainable redox-active materials, are promising storage
technologies that are cheaper and have fewer environmental hazards than the more mature
vanadium-based batteries (typically < 15 Wh/dm^3, vs. 20-35 Wh/dm^3, respectively)[2,3].
Unfortunately, they have shorter calendar lifetimes and lower energy-densities and
fundamental insight at the molecular level is thus required to improve performance[4,5]. Here we
report two *in situ* NMR methods to study flow batteries, which are applied on two separate
anthraquinones, 2,6-dihydroxyanthraquinone, DHAQ and 4,4'-((9,10-anthraquinone-2,6-
diyl)dioxy) dibutyrate, DBEAQ as redox-active electrolytes. In one method we follow the
changes of the liquids as they flow out of the electrochemical cell, while in the second, we
observe the changes that occur in both the positive and negative electrodes in the full
electrochemical cell. Making use of the bulk magnetisation changes, observed via the ^{1}H NMR
shift of the water resonance, and the linebroadening of the ^{1}H shifts of the quinone resonances
as a function of state of charge, we determine the potential differences of the two one-electron
couples, identify and quantify the rate of electron transfer between reduced and oxidised
species and the extent of electron delocalization of the unpaired spins over the radical anions.
The method allows electrolyte decomposition and battery self-discharge to be explored in real
time, showing that DHAQ is decomposed electrochemically via a reaction which can be
minimized by limiting the voltage used on charging. Applications of the new NMR metrologies
to understand a wide range of redox processes in flow and other battery systems are readily
foreseen.**

The two *in situ* NMR setups

Ex situ characterization of RFBs can be challenging due to the high reactivity, sensitivity to sample
preparation and short lifetimes of some of the oxidised and/or reduced redox-active molecules and
ions within the electrolytes. However, one of the distinct features of RFBs is the decoupling of
energy storage and power generation, providing different opportunities for *in situ* monitoring. To
date, methods such as *in situ* optical spectrophotometry[6] and Electron Paramagnetic Resonance
(EPR)[7] have been used to study, for example, crossover of quinones and vanadyl ions, but
considerable opportunities remain to improve characterization methods to address limitations
inherent to each method and to probe different phenomena. Nuclear Magnetic Resonance (NMR)
spectroscopy was used to study benzoquinone and polyoxometalate redox reactions in an *in situ*

49 static electrochemical cell[8-10]. Here, we move one step further by using NMR to study flow via two
50 different methods: probing the electrolyte in either the reservoir/flow path (*on-line* detection) or in
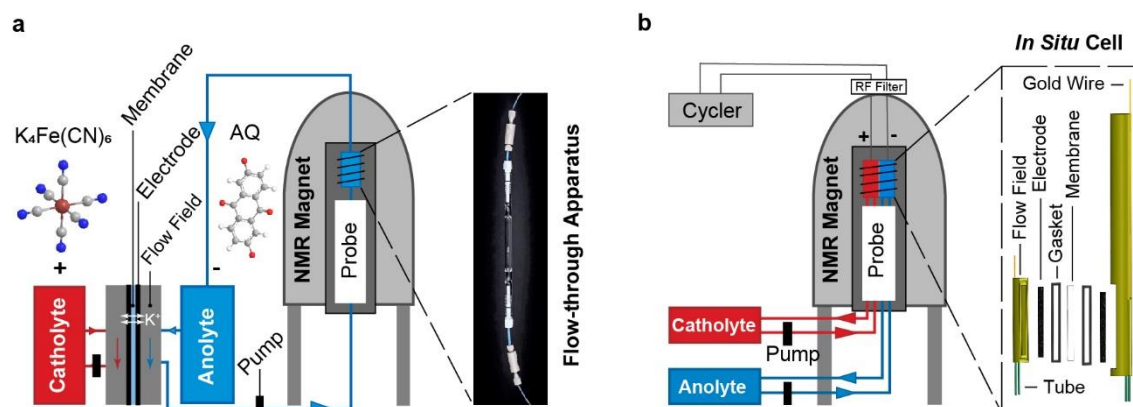51 the battery cell (*operando* detection).
52

Fig. 1. Schematics of the two *in situ* NMR setups. a, In the *on-line* setup, the battery
comprises of electrodes fabricated from SGL carbon felts with a 5.0 cm^2 active area, catholyte
and anolytes of potassium ferrocyanide and anthraquinones, respectively, dissolved in 1 M
KOH in D$_2$O. The volume of the flow path through the magnet including the sampling
apparatus (7.3 cm^3) and excluding the reservoir is 15.0 cm^3. At a flow rate of 13.6 cm^3/min,
the time of flight of the electrolyte out of and back into the reservoir is 1.1 min. **b**, In the
operando setup, the miniaturized flow cell (shown on the right) consists of flow fields, tubes to
flow electrolyte in and out, carbon electrodes, a cation-transport membrane and current
collectors. The volume of the flow path including the cell cavity (0.032 cm^3) is 7.8 cm^3. At a
flow rate of 2.5 cm^3/min, the time of flight of the electrolyte out of, and back into the reservoir
is 3.1 min.

53 In *on-line* detection (Fig. 1a and Extended Data Fig. 1a), the battery is positioned outside the NMR
54 magnet (300 MHz) and one electrolyte solution is pumped through a flow apparatus in the NMR
55 probe, enabling the study of the catholyte or anolyte separately. The setup requires minimum
56 modification of a lab-scale flow battery and can be easily adapted to other solution NMR instruments
57 and coupled with other analytical (flow) characterization methods. For *operando* detection (Fig. 1b
58 and Extended Data Fig. 1b), a miniaturized flow battery cell is positioned inside the detection region
59 of the NMR probe, enabling the study of the catholyte and anolyte simultaneously in the battery cell.
60 The majority of the data presented below are acquired with the *on-line* detection scheme unless
61 otherwise noted due to its higher sensitivity, the *on-line* setup having a larger sampling volume (7.3
62 cm^3) than the *operando* setup (0.032 cm^3). Furthermore, *on-line* detection provides superior
63 spectroscopic resolution (Extended Data Fig. 2) since there is no interference from the heterogeneous
64 (particularly the metallic) battery components, which lead to magnetic field inhomogeneities in the
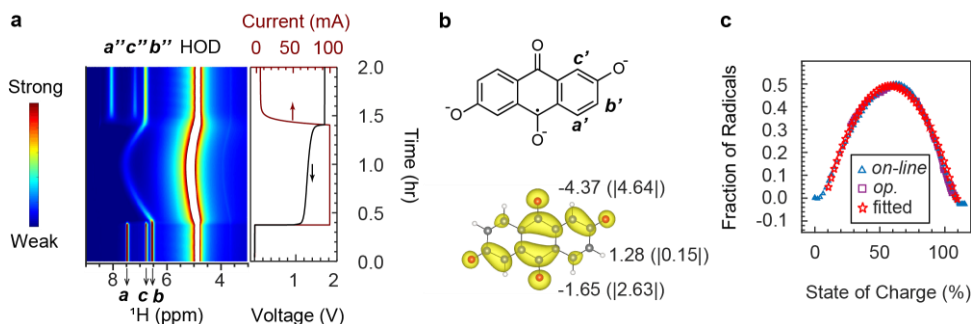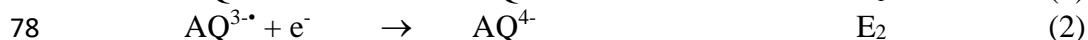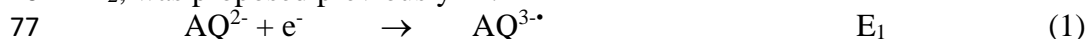65 *operando* setup[11,12].
66
67

**Fig. 2.** *In situ* **pseudo-2D ^{1}H NMR spectra acquired during electrochemical cycling.**
a, Spectra of 100 mM DHAQ against 300 mM $K_4Fe(CN)_6$ in a full cell with a current of 100 mA. The colour bar indicates the intensity of the resonances. The proton resonances are labelled ***a*** – ***c*** for DHAQ with single and double prime labels (e.g., ***a'*** and ***a''***) indicating the same protons in the singly and doubly reduced anions, respectively. The acquisition time per NMR spectrum used is 75 s and thus each spectrum is a snapshot of the electrochemical processes averaged over 2.1% SOC. **b**, Labeling of the protons, and DFT derived volumetric plot of the SOMO in DHAQ$^{3-\bullet}$. The values of the isotropic Fermi contact hyperfine coupling constants in MHz derived from DFT and EPR measurements (in brackets; the sign of the hyperfine interaction cannot be extracted from the experimental data, see Extended Data Fig. 3) are also shown for each unique proton. **c**, Experimentally determined fraction of DHAQ$^{3-\bullet}$ radicals as a function of SOC determined via the *on-line* and *operando* detection methods with a DHAQ concentration of 100 mM. The curve obtained from the *on-line* setup was fit with Eq. S6 and S7 (SI) to extract the equilibrium constant defining the radical and diamagnetic species' concentrations (K_c, Eq. 3).

Unravelling reaction mechanisms

On-line NMR measurements were performed for a full cell with 20 cm^3 of 100 mM anthraquinone and 300 mM potassium hexacyanoferrate (II), as the anolyte and catholyte, respectively. On charging at a constant current of 100 mA (20 mA/cm^2), corresponding to the reduction of the anthraquinones, the battery voltage increases from 1.2 V to the cut-off voltage of 1.7 V for DHAQ (Fig. 2a). Only one voltage step was observed, which is consistent with the cyclic voltammetry that reveals a single reversible redox peak centred at -0.68 V vs. SHE (Extended Data Fig. 4a). Despite the single peak, a two-step, one-electron process defined by the following reactions, with half-cell potentials of E_1 and E_2, was proposed previously[5,13]:

$$AQ^{2-} + e^- \quad \rightarrow \quad AQ^{3-\bullet} \qquad\qquad E_1 \qquad (1)$$
$$AQ^{3-\bullet} + e^- \quad \rightarrow \quad AQ^{4-} \qquad\qquad E_2 \qquad (2)$$

A chemical comproportionation reaction:

$$AQ^{2-} + AQ^{4-} \quad \rightleftharpoons \quad 2AQ^{3-\bullet} \qquad\qquad K_c \qquad (3)$$
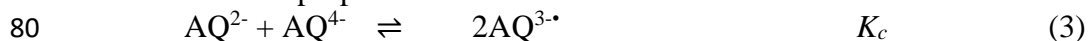
with an equilibrium constant, K_c, then occurs. This reaction controls the concentration of radicals in the solution throughout the electrochemical reactions; we note, however, that no direct spectroscopic evidence for radical formation and the complete reduction to AQ^{4-} has been observed to date.

Figure 2a presents the ^{1}H NMR spectra of DHAQ as a function of electrochemical cycling. Upon charging, the proton signals closest to the carbonyl redox centre (***a***, ***c***) disappear almost immediately while the proton signal farthest from the redox centre (***b***) broadens and moves toward higher chemical shifts. The apparent loss of signals (***a***, ***c***) is ascribed to electron delocalization over the semiquinone radical anion, which results in significant linebroadening[14,15]. As charging continues, the chemical shift of ***b*** reaches a maximum and then moves back toward lower values and narrows as the semiquinones continue to be further reduced. When the cut-off voltage is reached and the potential is held at 1.7 V, proton signals of the final diamagnetic product DHAQ^{4-} (***a''*** to ***c''***) appear. A similar trend was observed for DBEAQ^{2-} where the proton signals closest to the carbonyl redox

3

centre disappear almost immediately upon charging, while the proton signals farthest from the redox centre move toward higher chemical shift and then back to lower values until the signals of fully reduced $DBEAQ^{4-}$ appear (Extended Data Fig. 2d). Galvanostatic cycling reveals that these changes are reversible (Extended Data Fig. 5).

The broadening of proton resonances is related to the electron delocalization over the radical anion: the higher the electron density on the proton, the broader the peaks. Figure 2b shows the singly occupied molecular orbitals (SOMOs) for $DHAQ^{3-\bullet}$ determined by density functional theory (DFT) calculations, and the hyperfine coupling constants determined by EPR at a low concentration (1mM; Extended Data Fig. 3). The magnitudes of the EPR-derived hyperfine coupling constants, $\boldsymbol{b'}$ (|0.15| MHz) $<<$ $\boldsymbol{a'}$ (|2.63| MHz) $<$ $\boldsymbol{c'}$ (|4.64| MHz), are in agreement with the relative shifts and linebroadenings of the corresponding proton resonances. Differences between the hyperfine coupling constants determined by DFT and EPR are ascribed to errors inherent to the DFT method and the lack of inclusion of, for example, solvent effects (Extended Data Fig. 3). Of note, the shift of the water solvent resonance (measured here via the HOD signal present in the predominantly D_2O solvent) mirrors the behaviour of resonance $\boldsymbol{b}$ from $DHAQ^{2-}$ (Fig. 2a), the shift being ascribed to bulk magnetic susceptibility (BMS) effects, which are induced by changes in the magnetic susceptibility of the solution. The concentration of radicals can be readily estimated from this BMS shift by using the Evans' method (Eq. S8 to S16), a well-established NMR method for measuring the magnetic susceptibility of a solution[16]. Since the fraction of radicals is directly related to the comproportionation equilibrium constant K_c (reaction 3) and the state of charge (SOC) (Eq. S1-S7), the plot of radical concentration vs SOC can then be fit to the analytical expressions S6 and S7 (see Extended Data Fig. 4 for more in depth explanations) to extract K_c. The fit for DHAQ is shown in Fig. 2c, yielding a K_c of 3.72, corresponding to a potential separation ($E_1 - E_2$) of 33 mV (+/-10 mV at 293 K) (Eq. S4), in agreement with our CV model fitting (Extended Data Fig. 4h). The methods section (equilibrium concentrations of $DHAQ^{2-}$, $DHAQ^{3-\bullet}$ and $DHAQ^{4-}$, and CV fittings) discusses assumptions and errors associated with the two approaches for deriving ($E_1 - E_2$). Similar results are obtained via *on-line* and *operando* detection suggesting that the kinetics of the system is in equilibrium. In the *operando* experiment, the shift of the water resonances was only quantified (and converted into the radical concentration) after there is a clear peak separation between the water signals arising from DHAQ and $K_4Fe(CN)_6$ electrolytes (Extended Data Fig. 2a).

Determination of the intermolecular electron transfer rate

The rapid loss of proton signals $\boldsymbol{a}$ and $\boldsymbol{c}$ of $DHAQ^{2-}$ upon formation of fewer than 5% radicals (Fig. 2a) suggests a rapid intermolecular electron transfer process between the diamagnetic and paramagnetic ions, as described by the bimolecular reaction shown in Fig. 3a. NMR has been previously applied to study such processes[14,17,18]: suitable approximations have been derived allowing the electron transfer rate constants to be extracted from the peak broadening (see SI and ref. 19). In the slow exchange regime, the linebroadening is proportional to the electron transfer rate constant k_{ex} (Eq. S24), while in the fast exchange regime, the linebroadening is inversely proportional to k_{ex} (Eq. S25). As the temperature increases, linebroadening of proton signals in the slow exchange regime should increase, whereas linebroadening in the fast exchange regime should decrease or remain constant.

Variable-temperature (VT) *ex situ* NMR experiments were performed for a 100 mM DHAQ electrolyte solution containing 5 mM $DHAQ^{3-\bullet}$ radicals generated by electrochemical reduction (Fig. 3b and Extended Data Fig. 6), where the radical concentration was estimated by assuming that it is directly proportional to the applied charge. This assumption is valid at the beginning of the reduction/charge since the concentration of $DHAQ^{4-}$ is small (Extended Data Fig. 4e). As the temperature increases from 283.5 K to 313 K, the linewidths of peaks $\boldsymbol{a}$ and $\boldsymbol{c}$ increase, consistent with the slow exchange. The width of peak $\boldsymbol{b}$ largely remains essentially unchanged, suggesting that it is the fast exchange regime[19] (see Methods). The full width at the half maximum (FWHM) of

4

peaks *a* and *c* were then used to calculate the electron transfer rate constant, k_{ex}, under the slow exchange approximation, where the linebroadening (strictly the transverse relaxation rate) caused by exchange with the paramagnetic ions is given by the expression $R_{2p} = k_{ex}[P]$, where $[P]$ is the radical concentration. As shown in Fig. 3c, the plot of log k_{ex} vs. temperature calculated from peak *c* is linear while that for peak *a* deviates from linear behavior at elevated temperatures as proton *a'*, with its smaller electron spin density, approaches the intermediate exchange regime[19]. An activation energy of 0.46 eV for the electron transfer reaction between DHAQ^{2-} and DHAQ$^{3-•}$ is obtained which is larger than the DFT-derived values of 0.28 eV and 0.34 eV for electron transfer between sulfonated anthraquinones[20].
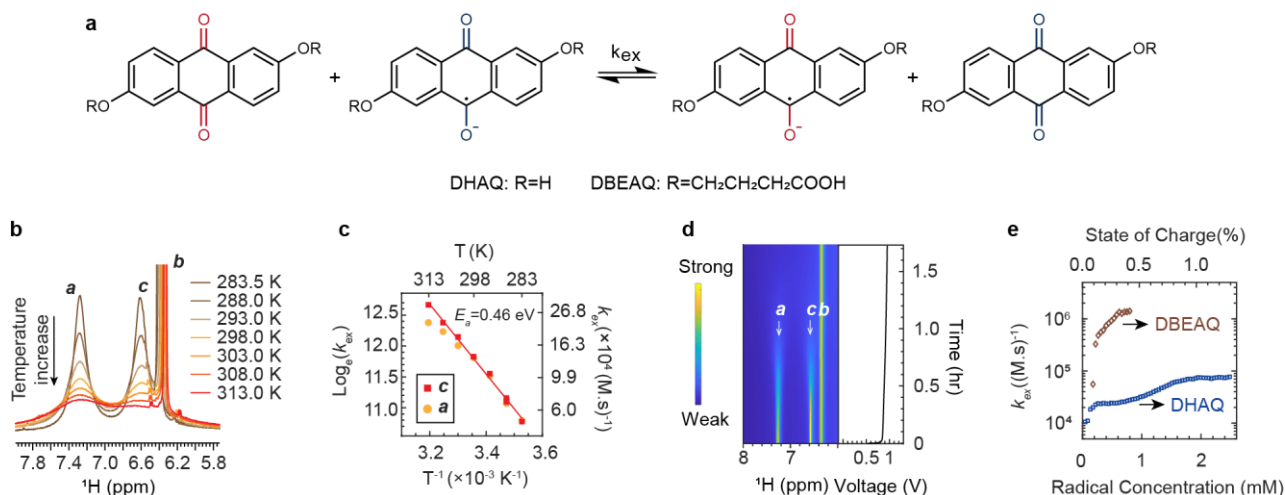

Fig. 3. NMR analyses of self-exchange electron transfer reactions. a, Self-exchange electron transfer reactions between oxidised and singly reduced AQs. **b**, Variable-temperature NMR spectra of 5 mM DHAQ$^{3-•}$ in a DHAQ solution of total concentration 100 mM. **c**, Arrhenius plot of the electron transfer rate constant, k_{ex}, calculated based on the FWHM of the DHAQ^{2-} peaks *a* (R^2=98.15%) and *c* (R^2=99.49%). **d**, *In situ* ^{1}H NMR spectra and voltage of the cell comprising 100 mM DHAQ and 300 mM K$_4$Fe(CN)$_6$, obtained with a low current of 1 mA so as to capture the initial stages of charging. **e**, k_{ex} calculated at different radical concentrations and SOC for 100 mM solutions of DHAQ and DBEAQ, respectively.

After validating the applicability of the slow exchange approximation, the self-exchange electron transfer processes are readily investigated *in situ* at room temperature (Fig. 3d and Extended Data Fig. 7). Electron transfer rate constants k_{ex} of approximately 1×10^5 and 1×10^6 (M.s)$^{-1}$ for DHAQ, and DBEAQ respectively, as shown in Fig. 3e and Extended Data Fig. 7i, were extracted from the broadening of peak *a* and *c* of DHAQ and *d* to *f* of DBEAQ. The changes in the calculated rate constants k_{ex} at the onset of reduction are ascribed to the inhomogeneous mixing of the low AQ$^{3-•}$ fraction ($< 1\%$) with AQ^{2-} as the electrolytes leave the reactor and flow through the tubing into the NMR magnet. Constant (equilibrium) k_{ex} values are obtained as the radical anions become homogeneously distributed as the reaction progresses, evidenced by the plateau at higher radical concentrations. The higher intermolecular electron transfer rate for DBEAQ is likely due to (i) the weaker intermolecular Coulombic repulsions between the DBEAQ anions, than between the DHAQ anions as the negative charges are more dispersed on DBEAQ than on DHAQ and (ii) the stronger van der Waals/hydrophobic interactions between the longer (non-polar) R groups in DBEAQ. The values of DHAQ and DBEAQ based on the *in* and *ex situ* NMR analysis are in the range of the previously reported values on other organic systems, spanning 10^4 to 10^{10} (M.s)$^{-1}$ [20-23].

Following electrolyte decomposition and battery self-discharge in real time

The *in situ* NMR approach allows us to follow electrolyte decomposition under specific cycling conditions. For example, for DHAQ, new ^{1}H NMR signals were observed at 6.5, 6.8, 7.1, 7.7 and 7.9 ppm during a potential hold at 1.7 V and complete reduction of the DHAQ (Fig. 4a). Based on *ex situ* 2D NMR correlation experiments and DFT-derived chemical shifts (Extended Data Fig. 8), these signals are assigned to the degradation products anthrone (DHA^{3-}) and anthrol ($DHAL^{3-}$), as identified previously[24]. Subsequent galvanostatic cycling of the solution without a potential-hold step did not change the signal intensity of DHA^{3-} and $DHAL^{3-}$ significantly (Extended Data Fig. 8e). In contrast, when the potential hold was reduced to 1.2 V, a much smaller concentration of decomposition products was detected (with peaks at 6.7, 7.1 and 8.1 ppm (Fig. 4a)), suggesting that the nature and extent of decomposition depends on the reduction potential. These observations suggest that the decomposition is an electrochemical reaction with a potential route outlined in Fig. 4c. A chemical disproportionation reaction with water, as previously proposed[24], cannot be excluded, the voltage dependence suggests that the products seen here are formed electrochemically. In contrast, for DBEAQ, no decomposition products were detected during a potential hold at 1.4 V and 1.7 V (Extended Data Fig. 9), in agreement with the work by Kwabi et al.[13] and with the proposal that degradation of DBEAQ instead occurs over long-term cycling via a mechanism involving nucleophilic attack rather than degradation of the reduced species[13].

The *in situ* NMR technique can be readily used to follow battery self-discharge. As shown in Fig. 4b, the open circuit voltage (OCV) of a charged battery (under the protection of flowing N_2 gas) decreases slowly from 1.3 V to 1.1 V and then after 17 hours, a sharp decrease to 0.5 V is seen. The *in situ* NMR spectra show that this is caused by the re-oxidation of $DHAQ^{4-}$ to $DHAQ^{3-\bullet}$ and $DHAQ^{2-}$. The rapid drop in OCV occurs when the $DHAQ^{2-}$ signals *a* and *b* reappear and sharpen, indicating that it is due to complete oxidation of the solution. To identify the potential oxidant, an *in situ* mass spectrometry technique based on the H-cell design was developed to monitor the gas evolution (Fig. 4d). A stepped potential experiment was performed from 1.2 to 2.1 V, stepping in increments of 0.1 V. D_2 evolution commences at 1.2 V and D_2 is steadily evolved both at higher potentials and during the rest periods. These two observations suggest that D_2 evolution originates from a chemical reaction, most likely from water reduction: $DHAQ^{4-} + 2D_2O \rightarrow DHAQ^{2-} + D_2 + 2OD^-$, noting that the redox potential of DHAQ is higher than that of the hydrogen evolution from water (-0.83 V vs SHE[13]) in a 1 M KOH aqueous solution making this reaction thermodynamically unfavourable (unless significant pH fluctuations occur). We cannot rule out the further reaction of the degraded electrolytes since there is considerable literature precedent for reactions of anthraquinone-based structures that involve hydrogen evolution, anthrone dimerization, for example, to form bianthrone being accompanied by hydrogen evolution[25]. In addition, some reported systems are photosensitive, providing another potential degradation route[26]. Further investigation into the various degradation mechanisms is in progress to understand how to control the stability of anthrahydroquinones in aqueous media.
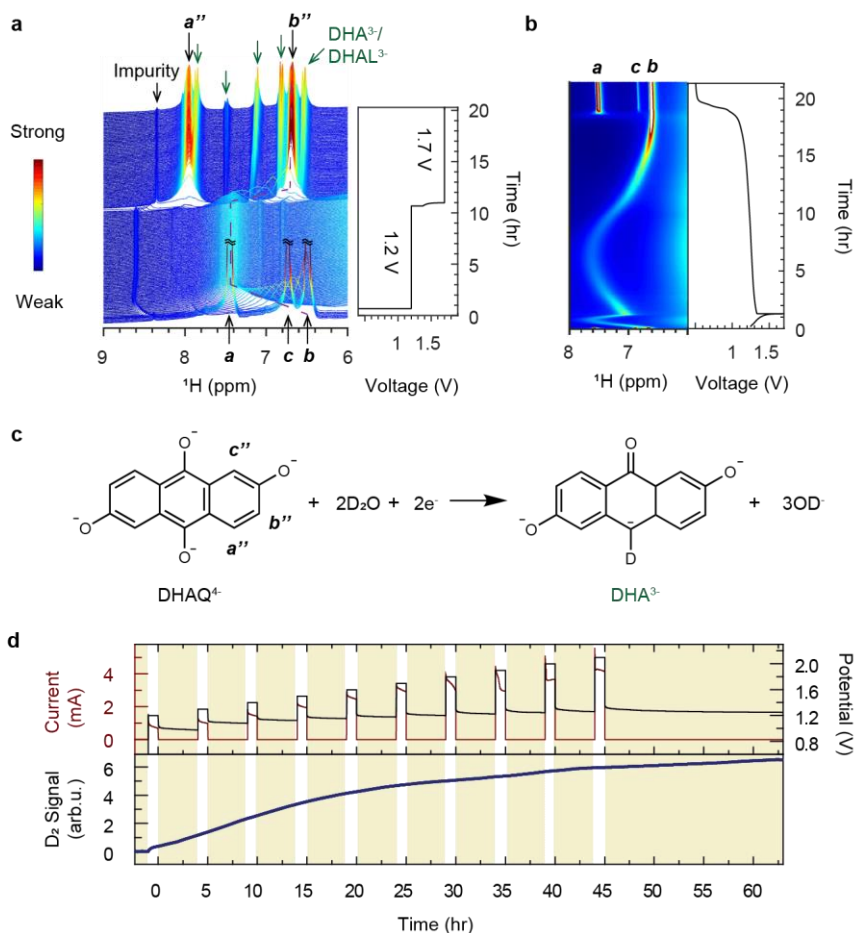
Fig. 4. *In situ* **NMR and MS analyses of electrolyte decomposition and battery self-discharge. a**, ^{1}H NMR spectra of 100 mM DHAQ during a potential hold at 1.2 V and 1.7 V, following charging at 100 mA. Green arrows highlight the DHA^{3-}/DHAL^{3-} signals. The purple dashed line tracks the signal of proton *b* and *b"*. The disappearance of signal *c"* is caused by an H-D exchange reaction with the D$_2$O solvent (Supplementary Fig. 2). **b**, ^{1}H NMR spectra, voltage and current of a 100 mM 2,6-DHAQ in D$_2$O in a charge-rest experiment in N$_2$ (flow) atmosphere. **c**, Proposed decomposition reaction of DHAQ^{4-}. **d**, *In situ* mass spectrometry signals of D$_2$ (m/z = 4) during a stepped potential-hold experiment (black line: potential, red line: current). The potential was increased from 1.2 to 2.1 V, stepping in increments of 0.1 V, holding for 1 hr at each potential step with an interleaved 4 hr rest period. 8 cm^3 of 100 mM DHAQ and 8 cm^3 of 300 mM K$_4$Fe(CN)$_6$ dissolved in D$_2$O are loaded in each electrolyte compartment of a custom-made H-cell.

210   In summary, we have demonstrated two *in situ* NMR metrologies to study flow batteries. The
211 formation of radicals and fully reduced anions is directly observed in two anthraquinone-based RFB
212 systems, their equilibrium concentrations being governed by the potentials of the two, one-electron
213 transfer redox processes. The radical concentration as a function of state of charge was quantified by
214 analysing the bulk magnetic susceptibility changes, allowing the voltage separation of the two
215 successive reductions to be extracted. The redox reaction was found to be coupled with electron
216 transfer between the radicals and diamagnetic anions, NMR spectroscopy providing a method to
217 measure the rates of these reactions. The presence of self-exchange electron transfer reactions in
218 organic flow batteries has significant implications because it will affect the overall rates of the redox
219 reactions, controlling, for example, the comproportionation rate. Electrochemically triggered
220 decomposition of DHAQ^{4-} to DHA^{3-}/DHAL^{3-} was observed under specific cycling conditions, but no
221 decomposition of DBEAQ^{4-} was observed. The real-time observation of re-oxidation of DHAQ^{4-} and

222 hydrogen evolution in these aqueous media indicates that other side reactions are occurring that
223 involves solvent water and/or degradation of DHAQ^{4-}. Because of the simplicity of the *on-line* NMR
224 setup, which consists essentially of a lab-scale RFB and a flow NMR sampling tube, we expect that
225 the wide adoption of this technique will advance the understanding of a variety of redox chemistries
226 in flow- and other battery systems. Beyond battery research, we demonstrate a new way to study
227 radical species, particularly at high radical concentrations when hyperfine coupling features in an
228 EPR spectrum are lost due to the electron spin interactions and electron transfer reactions. Our work
229 shows that, by following the spectral changes in real time, NMR can provide more key information
230 concerning molecular structure, spin density distributions and intermolecular electron hopping rates.

References:

231 1. Annual Energy Outlook 2018. *U.S. Department of Energy* (2018).
232 2. Wei, X. *et al.* Materials and systems for organic redox flow batteries: status and challenges. *ACS Energy Letters*
          2, 2187-2204 (2017).
235 3. Leung, P. *et al.* Recent developments in organic redox flow batteries: A critical review. *J. Power Sources* **360**,
          243-283 (2017).
237 4. Yang, B., Hoober-Burkhardt, L., Wang, F., Surya Prakash, G. K. & Narayanan, S. R. An inexpensive aqueous
          flow battery for large-scale electrical energy storage based on water-soluble organic redox couples. *J.
          Electrochem. Soc.* **161**, A1371-A1380 (2014).
240 5. Lin, K. *et al.* Alkaline quinone flow battery. *Science* **349**, 1529-1532 (2015).
241 6. Tong, L. *et al.* UV-Vis spectrophotometry of quinone flow battery electrolyte for in situ monitoring and
          improved electrochemical modeling of potential and quinhydrone formation. *Phys. Chem. Chem. Phys.* **19**,
          31684-31691 (2017).
244 7. Lawton, J. S., Aaron, D. S., Tang, Z. & Zawodzinski, T. A. Electron spin resonance investigation of the effects
          of vanadium ions in ion exchange membranes for uses in vanadium redox flow batteries. *ECS Trans.* **41**, 53-56
          (2012).
247 8. Webster, R. D. In situ electrochemical-NMR spectroscopy. Reduction of aromatic halides. *Anal. Chem.* **76**,
          1603-1610 (2004).
249 9. Friedl, J. *et al.* Asymmetric polyoxometalate electrolytes for advanced redox flow batteries. *Energy Environ.
          Sci.* **11**, 3010-3018 (2018).
251 10. Cao, S.-H. *et al.* In situ monitoring potential-dependent electrochemical process by liquid NMR
          spectroelectrochemical determination: a proof-of-concept study. *Anal. Chem.* **89**, 3810-3813 (2017).
253 11. Pecher, O., Carretero-González, J., Griffith, K. J. & Grey, C. P. Materials' methods: NMR in battery research.
          Chem. Mater. **29**, 213-242 (2017).
255 12. Wang, H. *et al.* In situ NMR spectroscopy of supercapacitors: insight into the charge storage mechanism. *J. Am.
          Chem. Soc.* **135**, 18968-18980 (2013).
257 13. Kwabi, D. G. *et al.* Alkaline quinone flow battery with long lifetime at pH 12. *Joule* **2**, 1894-1906 (2018).
258 14. de Boer, E. & MacLean, C. NMR study of electron transfer rates and spin densities in p-xylene and p-
          diethylbenzene anions. *J. Chem. Phys.* **44**, 1334-1342 (1966).
260 15. Pell, A. J., Pintacuda, G. & Grey, C. P. Paramagnetic NMR in solution and the solid state. *Prog. Nucl. Magn.
          Reson. Spectrosc.* **111**, 1-271 (2019).
262 16. Evans, D. F. The determination of the paramagnetic susceptibility of substances in solution by nuclear magnetic
          resonance. *J. Chem. Soc. (Resumed)*, 2003-2005 (1959).
264 17. Johnson. Jr., C. S. Nuclear transverse relaxation in electron-transfer reactions. *J. Chem. Phys.* **39**, 2111-2114
          (1963).
266 18. de Boer, E. & MacLean, C. Spin densities in the alkyl groups of alkyl-substituted naphthalene negative ions,
          determined by N.M.R. *Mol. Phys.* **9**, 191-193 (1965).
268 19. Bertini, I., Luchinat, C., Parigi, G. & Ravera, E. in *Chapter 6, NMR of Paramagnetic Molecules (Second
          Edition)*151-173 (Elsevier, 2017).
270 20. Rosso, K. M., Smith, D. M. A., Wang, Z., Ainsworth, C. C. & Fredrickson, J. K. Self-exchange electron transfer
          kinetics and reduction potentials for anthraquinone disulfonate. *J. Phys. Chem. A* **108**, 3292-3303 (2004).
272 21. Grampp, G., Galán, M. & Sacher, M. Kinetics of Photoinduced Electron Transfer Reactions of Some
          Anthraquinone Radical Anions with Various Inorganic Ions: Comparison with Marcus Cross-Relation. *Ber.
          Bunsenges. Phys. Chem.* **99**, 111-117 (1995).
275 22. Rosokha, S. V. & Kochi, J. K. Continuum of Outer- and Inner-Sphere Mechanisms for Organic Electron
          Transfer. Steric Modulation of the Precursor Complex in Paramagnetic (Ion-Radical) Self-Exchanges. *J. Am.
          Chem. Soc.* **129**, 3683-3697 (2007).

278 23. Meisel, D. & Fessenden, R. W. Electron exchange and electron transfer of semiquinones in aqueous solutions. *J.*
279   *Am. Chem. Soc.* **98**, 7505-7510 (1976).
280 24. Goulet, M.-A. *et al.* Extending the lifetime of organic flow batteries via redox state management. *J. Am. Chem.*
281   *Soc.* **141**, 8014-8019 (2019).
282 25. Donovan, P. M. & Scott, L. T. 4,11-bisanthenequinone and 10, 10'-bianthrone: simple one-step syntheses from
283   anthrone. *Polycyclic Aromat. Compd.* **28**, 128-135 (2008).
284 26. Filipescu, N., Avram, E. & Welk, K. D. Photooxidative transformations of anthrone, bianthronyl, and
285   bianthrone in acid solution. *J. Org. Chem.* **42**, 507-512 (1977).

METHODS

Materials and synthesis. 2,6-dihydroxyanthraquinone (2,6-DHAQ, A89502 technical grade, 90% purity), potassium hexacyanoferrate(II) trihydrate (P3289, $\geq$ 98.5% purity), D_2O (151882, 99.9 atom %) and ethyl 4-bromobutyrate (167118, 95%) were purchased from Sigma Aldrich Chemicals. Anhydrous N, N-dimethylformamide (43465, $\geq$ 99.9% purity), potassium ethoxide (14263.30, $\geq$ 95% purity), anhydrous potassium carbonate (A16625, $\geq$ 99.0% purity), isopropanol (20839.366, $\geq$ 99.0% purity), and glacial acetic acid (20103.364, 99-100%) were purchased from VWR.

4,4'-((9,10-Anthraquinone-2,6-diyl)dioxy)dibutyric acid (2,6-DBEAQ) was synthesized following the previously reported method[13]. 2,6-DHAQ (5.00 g, 20.8 mmol) was dissolved in anhydrous DMF (250 cm^3) and potassium ethoxide (6.13 g, 72.8 mmol) added to the solution under vigorous stirring. The mixture was stirred at room temperature for 15 min. To this, anhydrous K_2CO_3 (14.40 g, 104.2 mmol) and ethyl 4-bromobutyrate (21.41 g, 109.8 mmol) were added and the mixture solution was then heated to 95 °C for 23 h. The reaction mixture was poured into deionized water, and the solid collected by filtration, washed with deionised water and dried in a vacuum oven overnight to afford diethyl 4,4'-((9,10-anthraquinone-2,6-diyl)dioxy)dibutyrate (2,6-DEDBEAQ, 9.20 g, 94.2%), the ester precursor of 2,6-DBEAQ, as silver-grey powders. 2,6-DEDBEAQ (1.00 g, 2.13 mmol) was hydrolysed in 0.15 M KOH water-isopropanol (2:1 v/v) solution (60 cm^3) at 60 °C for 12 h. The reaction mixture was poured into deionized water (200 cm^3) and glacial acetic acid added dropwise to adjust the pH to 4. The solid was collected by filtration, washed with deionised water and dried in a vacuum oven overnight to afford 2,6-DBEAQ in a quantitative yield. The NMR spectra that were subsequently acquired were consistent with previously reported spectra[13].

Flow battery assembly. The hardware of the flow battery was purchased from Scribner Associates. Ultra-high purity and sealed graphite flow plates with serpentine flow patterns were used for both electrodes. Each electrode comprised of a 4.6 mm or 6.0 mm SGL carbon felt with 5 cm^2 active area. Nafion® 212 was used as the ion transport membranes. Pretreatment of Nafion® 212 membrane was performed by first heating the membrane in 80 ºC de-ionized water for 20 minutes and then soaking it in 5% hydrogen peroxide solution for 35 minutes. The treated membranes were stored in 0.1 M KOH solution at room temperature. PTFE frames with a thickness of 3 mm were used to position the electrodes with Viton gaskets of 0.7 mm in thickness on each side of the frames. The current collectors are gold-plated copper plates. Anodized aluminum end plates with reactant input/output ports were used, however, it was found that the coatings were easily corroded by basic solutions. Direct solution contact was avoided by carefully inserting the inlet and outlet tubing through the Viton O-ring seals.

A stock solution of 1 M KOH dissolved in D_2O was prepared and used as the solvent. On the negative side, either 200 mM (in 1.4 M KOH), 100 mM, 50 mM, and 30 mM 2,6-DHAQ was prepared in 20 cm^3 solvent. The SOC of the battery was calculated by dividing the number of electrons that have flowed from the electrochemical cycler by the theoretical storage capacity of the quinone anions assuming a two electron per anion redox process. For example, for a 100 mM DHAQ of 90% purity, the theoretical capacity is 96.5 mA.hr. On the positive side, potassium hexacyanoferrate(II) trihydrate was dissolved in 20 cm^3 solvent to form a 300 mM solution; this corresponds to 1.5 times the total capacity of the 100 mM 2,6-DHAQ solution for the same volume of electrolyte. When the battery undergoes

9

galvanostatic cycling, 50 mM potassium hexacyanoferrate(III) is added to the positive side to ensure that both Fe^{2+} and Fe^{3+} are in excess during battery cycling.

Custom-made glassware, made from Pyrex, with gas inlet, outlet, liquid inlet and outlet were used as electrolyte reservoirs. Prior to the experiments, all solutions were degassed with N_2 gas rigorously for 30 minutes to an hour. The torque applied on the bolts that tighten the cell was found to affect the battery performance significantly. It was optimized at 2 N.m on each bolt. The galvanostatic cycling of the battery was controlled by a portable Bio-Logic SAS (Model: SP-150).

***On-line* NMR setup.** A 10 mm O.D. custom-made medium-wall flow-through NMR sampling tube of 14 cm in length is positioned in a Bruker 2.5 micro-imaging probe (Extended Data Fig. 1a). The electrolyte solution flows from the bottom to the top of the tube. The inlet and outlet of the sampling tube were connected to two 1/16″ PFA tubes (0.5 mm I.D.) of 3 m in length via 1/16″ to 1/8″ tube adaptors. The PFA tube at the bottom is connected to the outlet of the battery; the PFA tube at the top is connected to the inlet of the electrolyte reservoir. The electrolyte is pumped through the sampling tube and the flow battery which is positioned next to a 300 MHz NMR magnet outside the 5 Gauss line by a peristaltic pump (Cole-Parmer, MasterFlex® L/S®, model No. 07551-20; Pump head model No. 77202-60; MasterFlex tubing Chem Bio #14). The volume of the electrolyte inside the NMR sampling tube is 7.3 cm^3. The volume of the electrolyte in the PFA tubes is 1.2 cm^3. The volume of the electrolyte that passes through the MasterFlex tube is 6.5 cm^3. Based on an I.D. of 8.16 mm of the sampling tube and 3 cm of the detection length by the NMR probe, the effective volume detected by NMR is 1.57 cm^3. Flow rates were measured at different rotary speeds of the pump using the same tubing, as shown in Extended Data Fig. 1d. At a flow rate of 13.6 cm^3/min, the electrolyte takes 60 s to flow back to the reservoir, so the time lag between the electrochemical cycling and the NMR detection is 30 s.

As shown in Extended Data Fig. 1c, pseudo-2D NMR experiments were performed by direct excitation with a 90° pulse. The acquisition time is 1.5 s. Each spectrum has 8 scans (number of scans, ns). A time delay, d_2, after the eight scans is set before the next spectrum acquisition starts. With a recycle delay of 7 s and a time delay, d_2, of 7 s, the total acquisition time of a spectrum is 75 s ((7+1.5)×8+7=75). Due to the high ionic conductivity of the basic solution, the 90° pulse width for proton increases from 20 μs, for a non-conductive solution, to 27 μs at an RF power of 30 W. Pulse calibration was performed as a function of SOC and the 90° pulse width remains the same. All spectra were referenced to the water chemical shift at 4.79 ppm before battery cycling starts. The spectral widths were 200 or 20 ppm. Peak assignment was facilitated by the J-coupling interactions among the three aromatic protons: H (J_{ab}) = 8.6 Hz, H (J_{bc}) = 2.5 Hz.

***Operando* NMR setup.** The *in situ* cell assembly consists of six key components: the PEEK flow field, carbon electrode, an ion transport membrane, current collectors, a PEEK sleeve, PEEK tubes (flow inlet and outlet). Pictures of the *in situ* cell are shown in Extended Data Fig. 1b. The diameter of the cell assembly is 9.9 mm, which fits into a Bruker 2.5 micro-imaging probe. The structures of the catholyte and anolyte compartment are identical except for an extended solid part of 12.20 cm in length attached to one compartment, which is held in the NMR probe by a screw cap. The flow field inside the electrolyte compartment is 1.80 cm in length, 0.40 cm in width and 500 μm in depth. A layer of carbon electrode (Sigracet®, 39AA, 80% porosity) of 1.80 cm in length, 0.40 cm in width and 280 μm in thickness is placed inside the flow field. A current collector made of two gold wires of 0.5 mm in O.D. and 16.0 cm in length passes through a hole at the back of the flow field and is in electrical contact with the carbon electrode. The other end of the current collector is connected to an electrical cable that passes through a DC-5 MHz low pass filter at the top of the NMR magnet and connects to the electrochemical cycler. A treated Nafion® 212 membrane of 2.80 cm in length, 0.80 cm in width and 50.8 μm in thickness is compressed between the catholyte and anolyte compartment by Viton O-rings. The cell assembly is held in a PEEK sleeve of 0.99 cm O.D. and

376   0.89 cm I.D. The electrolyte inlet and outlet on each compartment are PEEK tubes (1/16″ O.D.) of

377   10 cm in length. They are connected to 1/16″ PFA tubes of 3 m in length via 1/16″ to 1/16″ unions,

378   which pass through the bottom of the NMR probe. The PFA tube is connected to a peristaltic pump

379   (Cole-Parmer, MasterFlex® L/S®, model No. 07551-20; Pump head model No. 77202-60;

380   MasterFlex tubing Chem Bio #14), and then to the electrolyte reservoir. The total volume of

381   electrolyte in the PFA tubes is 1.2 cm^3. The volume in the MasterFlex tube on the pump is 6.5 cm^3.

382   At a flow rate of 2.5 cm^3/min, the electrolyte takes 185 s to flow back to the reservoir, so the time lag

383   between the electrochemical cycling and the NMR detection is 92 s. The effective NMR detection

384   volume in the *in situ* cell is 0.032 cm^3 (excluding the volume of carbon electrode) and therefore the

385   residence time in the detection region of the NMR probe is 0.8 s. Pseudo-2D NMR experiments were

386   performed with a 90° pulse of 27 μs, an acquisition time of 0.15 s, a recycle delay, d$_1$ of 1 s, and a d$_2$

387   of 1 s. Each spectrum has 64 number of scans. The total acquisition time of a spectrum is 75 s

388   ((1+0.15)×64+1=74.6).

389   ***In situ* relaxation measurements.** The longitudinal (T$_1$) and transverse (T$_2$) relaxation

390   measurements were performed *in situ* via the *on-line* setup. A full battery of 20 mL 100 mM DHAQ

391   and 40 mL 200 mM K$_4$Fe(CN)$_6$ were charged at 100 mA to the cut-off potential of 1.7 V. The

392   potential was then held at 1.7 V for 40 mins. A flow rate of 13.6 cm^3/min was used. The flow and

393   electrochemical cycling were paused intermittently (every 5 or 10 minutes, see Extended Data

394   Fig. 10) during charging, and the relaxation measurements were performed on a static solution. The

395   90° pulse width was calibrated before each measurement and was found to be the same throughout

396   the electrochemical cycling. After each relaxation measurement, flow and electrochemical cycling

397   were resumed. The relaxation measurement at each SOC takes up to 30 mins, which is much shorter

398   than the time for the re-oxidation of DHAQ (17 hrs). There was no noticeable change of chemical

399   shift before and after each measurement, suggesting that the reduced DHAQ is stable on the time

400   scale of the relaxation measurement. Nonetheless, there will be errors arising from the re-oxidation

401   and decomposition of DHAQ during the measurement, particularly at high SOC (as discussed in the

402   main text). The errors are reflected in the data fitting and are shown in Extended Data Fig. 10b,c.

403   T$_1$ relaxation measurements were performed with an inversion-recovery (t1ir) pulse sequence

404   comprising 180° and a 90° pulses, with an increasing delay time (t) between the two pulses for each

405   spectrum in the second dimension. Eight to sixteen spectra were acquired in the second dimension. A

406   recycle delay of 30 s was applied for the oxidized DHAQ. As the T$_1$ time of proton **b** in DHAQ in the

407   presence of radicals is an order of magnitude shorter than that of HOD, two separate measurements

408   were performed on DHAQ proton **b** and HOD, with a recycle delay of 0.5 s and 2 s used for each

409   molecule. The signal integral I(t) was plotted as a function of t, and fit by $I(t) = I_0(1 - 2e^{t/T_1})$.

410   T$_2$ relaxation measurements were performed with a Carr-Purcell-Meiboom-Gill (CPMG) pulse

411   sequence comprising a 90° pulse, and a train of 180° pulses, with a delay time of 1 ms before and after

412   each 180° pulse. Eight to sixteen spectra were acquired in the second dimension, with increasing

413   number (up to 2000) of 180° pulses. The signal integral I(t) was plotted as a function of the sum of the

414   delay time, t, and fit with $I(t) = I_0 e^{-t/T_2}$.

415   T$_1$ relaxation times for H^a, H^b, H^c and HOD were measured to be 1.6 $\pm$ 0.2, 1.9 $\pm$ 0.2, 4.9 $\pm$ 0.2 and

416   13 $\pm$ 1 s respectively. Of note, these T$_1$ times depend on the protonation level of the deuterated solvent

417   as the relaxation is largely driven by proton dipolar coupling interaction for the diamagnetic solutions.

418   Shorter T$_1$ relaxation values for H$^{a"}$, H$^{b"}$, H$^{c"}$ on the fully reduced DHAQ^{4-} anion were measured to be

419   0.32 $\pm$ 0.06, 0.34 $\pm$ 0.07, and 0.22 $\pm$ 0.08 s, but these were measured in the presence of radicals, i.e.,

420   in the *in situ* experiments. T$_1$ and T$_2$ times were then measured as a function of SOC. Extended Data

421   Fig. 10a presents the voltage profile of a full battery of 100 mM DHAQ and 200 mM K$_4$Fe(CN)$_6$

422   during intermittent charging with a current of 100 mA. Extended Data Fig. 10b shows that the

423   measured HOD T_1 and T_2 values both decrease rapidly on charging to a SOC of 9%, T_1 decreasing
424   from 13.1 s to below 0.7 s, and T_2 from 5.1 s to below 0.5 s. The changes are more gradual thereafter,
425   reaching a minimum of 0.1 s (for both T_1 and T_2) at 50 - 70% SOC. They then increase to 0.4 s as the
426   battery is charged to its full capacity. The T_1 value of **b** follows the same trend as that of HOD,
427   decreasing from 1.9 s to below 0.03 s at a SOC of 9% (Extended Data Fig. 10c).

428   **Effect of flow rate, radical concentration and relaxation times on magnetisation build-up and**
429   **linebroadening.** Under flow conditions, the build-up of magnetisation of the nuclear spins is
430   determined by the time that the electrolyte molecules spend in the high magnetic field[27]. Since $5T_1$
431   allows a build-up of 99.3% of the maximum thermal polarization, ideally a residence time of the
432   electrolyte in the field, τ, should be longer than $5T_1$. τ is related to the flow rate, υ, by $\tau = V/\upsilon$,
433   where V is the volume of electrolyte in the high magnetic field. Setting V to be the same as the
434   detection volume of the NMR probe gives the lower limit of the residence time, since the region of
435   high magnetic field extends to a longer length than the detection region of the NMR probe. In the *on-*
436   *line* setup, the volume of the detection region is 1.57 cm^3. A residence time of $5T_1$ of the DHAQ
437   protons H^a (1.5 s), H^b (1.9 s), H^c (4.9 s) and HOD (13 s) requires flow rates lower than 12.6, 9.9, 3.8
438   and 1.4 cm^3/min, respectively, for quantitative measurements of the diamagnetic species in the
439   absence of any radicals. In the *operando* cell, the detection volume is 0.032 cm^3 and a residence time
440   of $5T_1$ for H^a, H^b, H^c and HOD gives flow rates of 0.3, 0.2, 0.1 and 0.03 cm^3/min, respectively. We
441   note that if faster flow rates are required, simple methods for polarizing the nuclear spins before the
442   liquids actually enter the rf coil (e.g., by adding loops or liquid reservoirs in the magnet) can be
443   readily added to the set-up.

444   Extended Data Fig. 10d,e show the ^{1}H NMR spectra of DHAQ and HOD as a function of flow rate
445   without electrochemically cycling the battery in the *on-line* setup. The signal integral is plotted
446   against the flow rate, as shown in Extended Data Fig. 10f,g. As flow rate increases, the decrease of
447   the water signal is the most pronounced because of its long T_1 value, followed by proton **c** of DHAQ.
448   Signal intensity of **a** and **b** is almost unaffected by the flow rates studied here due to the shorter T_1
449   values of H^a and H^b. Of note, when radical species, e.g. DHAQ$^{3-\bullet}$ are generated, the T_1 will be
450   shortened substantially due to the nuclei-electron spin interactions and much higher flow rates will
451   be possible without reducing the signal intensity.

452   To achieve optimized electrochemical performance of the battery system, i.e. a low overpotential, a
453   high flow rate is desirable to drive the system out of the mass transport-limited regime. Given the
454   detection volume of 1.57 cm^3 and 0.032 cm^3 in the *on-line* and *operando* setup, flow rates that allow
455   quantitative measurements of DHAQ proton **b** in the presence of small concentrations of radicals,
456   and allow a residence time of $> 5T_1$ (5×0.03 s), correspond to < 628.0 cm^3/min and < 14.4 cm^3/min,
457   respectively. The flow rates in the majority of the *on-line* and *operando* NMR experiments are set to
458   13.6 cm^3/min and 2.5 cm^3/min, respectively, which are in this quantitative regime.

459   During NMR data acquisition, the thermal polarization is converted into transverse magnetization
460   by a 90° RF pulse, and the decay of the transverse magnetization (T_2 relaxation) determines the
461   linewidth of the NMR signal. There is a finite probability that a fraction of the spins with transverse
462   magnetization will leave the detection region before the data acquisition finishes, which may cause
463   further linebroadening. The longer the T_2 time, the more susceptible the signal is to linebroadening
464   from flow. The FWHM of the DHAQ and the HOD signals as a function of flow rate is plotted in
465   Extended Data Fig. 10h. As the flow rate increases from 13.6 cm^3/min to 37.5 cm^3/min, the HOD
466   FWHM increases slightly from 6 to 7 Hz while the FWHM of the DHAQ signals show negligible
467   change. In the presence of the DHAQ$^{3-\bullet}$ radicals, which are produced during battery cycling, the T_2 is
468   shortened and thus the effect of flow on the linewidth of the DHAQ proton signals is further reduced.

Study of H-D exchange by *ex situ* NMR. A solution of 100 mM 2,6-DHAQ dissolved in 1 M KOH in D$_2$O was prepared and left in an ambient environment for 30 days before taking the first NMR spectrum. The same solution was then charged (corresponding to the electrochemical reduction of 2,6-DHAQ) in a redox flow battery and a 0.5 cm^3 aliquot was extracted. The aliquot was transferred to a 5 mm thin-wall NMR tube and 1D NMR spectra were acquired on a 500 MHz solution NMR spectrometer. For ^{1}H NMR, 32 scans were accumulated with a 30$^\text{o}$ pulse and a recycle delay of 1 s. For ^{13}C NMR, 1024 scans were accumulated with a 30$^\text{o}$ pulse and a recycle delay of 3 s.

Study of electron transfer reactions by variable-temperature ^{1}H NMR experiments. The solvent of 1 M KOH in D$_2$O was degassed by Ar gas for 2 hours. A H-cell was assembled inside the glovebox as described below for the charge-rest experiments. 20 cm^3 of 100 mM DHAQ solution was first reduced at 10 mA for 30 minutes (9 mM radicals) and a 0.1 cm^3 aliquot was extracted and sealed in a 5 mm thick-wall NMR tube with an air-tight Young's tap. Then the DHAQ was oxidised at 1 mA for 140 minutes (5 mM of radicals) and an NMR sample was prepared in the same way as for the 9 mM radicals.

NMR spectra were acquired on a 500 MHz solution NMR spectrometer using a one pulse (90$^\text{o}$) sequence. For the spectra acquisitions of the sample containing 5 mM of radicals, the temperature of the NMR probe was ramped up, from 283 K to 313 K in increments of 5 K and cooled down to 288 K while spectra were acquired at each temperature. The heating was carried out in this way to ensure that any the re-oxidation of the solution did not perturb the measurement. For the spectral acquisition of the sample containing 9 mM radicals, the temperature was set at 283 K, then ramped up from 288 K to 338 K in increments of 10 K. As the magnetic field was locked on the water resonance at 4.79 ppm and the water resonance is temperature-dependent, the shift of peak *a* of DHAQ was manually set at 7.3 ppm after acquisition to allow for a ready comparison of the different spectra.

As shown in the EPR results (Extended Data Fig. 3), the magnitudes of the hyperfine coupling of the three protons are *b'* (0.15 MHz) $<<$ *a'* (2.63 MHz) $<$ *c'* (4.64 MHz). Due to the much smaller hyperfine coupling constant, resonance *b/b'* is in the fast exchange regime while resonances *a/a'* and *c/c'* are in the slow-exchange regime. This is also manifested by the VT NMR experiments shown in Extended Data Fig. 6b,c where the linewidth of resonance *b* is largely insensitive to the changes in temperature and electron transfer rate.

To verify the dependence of linewidth on the exchange rate, k_{ex}, the effect of two-site chemical exchange on the spectra was simulated with the programme *Spinach*[28]. In the simulation, the concentration of radicals was set to either 5 mM or 9 mM, which is the same as the radical concentration used in the VT experiments. The position of resonance *b'* of 7.51 ppm was used, which is estimated from the shift of *b* in the *on-line* NMR spectra (Fig. 2a) at low radical concentrations. For example, in the presence of 1.35% radicals (as determined by the shift of the water resonance via the Evans' method), the shift of *b* is 6.4645 ppm, and the shift of *b'* is given by:

$$(6.4645 - 98.6 \times 6.45)/1.35 \text{ ppm} \qquad [1]$$

where 6.45 ppm is the shift of resonance *b* without the presence of radicals.

To illustrate that the exchange is indeed in the fast exchange limit, we varied the exchange rate constant, k_{ex}, from 0 to 10^6 (M.s)$^{-1}$. Coalescence of resonances *b* and *b'* occurs at approximately 10^4 (M.s)$^{-1}$ and a superposition of the spectra obtained with $k_{ex} = 0.5 \times 10^5$ to 10^6 (M.s)$^{-1}$ show only negligible changes in linewidth, consistent with our suggestion that exchange is indeed in the fast regime for these values of k_{ex}. We shall refer to the coalesced resonance as *b/b'*. k_{ex} was then set to

513 either 0.50×10^5, 1.05×10^5 or 3.0×10^5 (M.s)$^{-1}$ in the simulations, which corresponds to the measured

514 values at 283.5, 293.0 and 313.0 K from the VT experiment (Fig. 3c; extracted from the analysis of

515 resonances **a** and **c**). As the temperature increases, the FWHM of resonance **b/b'** decreases from 16.7

516 to 13.9, to 10.7 Hz in the simulations. The experimental spectra (Extended Data Fig. 6b) are more

517 complex because they contain J coupling. Deconvolution of the resonances, however, indicates that

518 the broadening decreases from 3.3 to 3.2, then to 2.9 Hz. On increasing the radical concentration to

519 9 mM, the simulated linebroadenings decrease from 29 to 19 Hz, with the same exchange rates,

520 while experimentally, the linewidth decreases from 24.1 to 23.5 Hz. Although our simulations are in

521 reasonable agreement with experiment, they predict slightly larger broadenings than seen

522 experimentally, with larger errors being observed with lower concentrations of radicals. This is

523 ascribed to: (a) uncertainty in the T_1 of resonance **b'**: decreasing this value from 500 Hz (the value

524 chosen for the original simulations) to 50 Hz decreases the linebroadening of resonance **b"** from 13.9

525 to 7.7 Hz for $k_{ex} = 1.0 \times 10^5$ (M.s)$^{-1}$ and 5 mM radical concentration; (b) uncertainty in the shift of **b**

526 as charging progresses and the pH changes – only very small changes will have a *significant* effect

527 on the linebroadening since the shift difference between **b** and **b'** is so small. To address this at least

528 in part we estimated the shift of **b'** at the beginning of charge where pH and BMS effects are likely to

529 be smaller; (c) the lack of inclusion of the effect of temperature on the shift of **b'** (and **b**) and their

530 relaxation times.

531 **Identification of the DHAQ decomposition products.** The following NMR experiments were

532 performed on a 0.2 cm^3 aliquot solution taken from the H-cell experiments at 470 hours (which was

533 the end of a charge-rest experiment), and sealed in a 5 mm NMR tube (see section *H-Cell*

534 *experiments in an Ar glovebox*).

535 *^{1}H diffusion-ordered spectroscopy (DOSY)* spectra were performed with a 2D sequence for diffusion

536 measurements using stimulated echo and longitudinal eddy current decay using bipolar gradient

537 pulses[29]. The diffusion coefficients were calculated following:

$$f(g) = I_o \times e^{-\gamma g^2 \delta^2 (\Delta - \delta/3)D}$$

[2]

539 where I_o is the peak integral without pulse field gradients, γ is the gyromagnetic ratio of a proton

540 i.e. 26752 rad/(s.Gauss), g is the variable gradient strength from 0 to 2100 Gauss/cm, with 16

541 increments of gradient strength. The length of the gradient δ is 1.5 ms and the diffusion time Δ is

542 100 ms.

543 *^{1}H homonuclear correlation spectroscopy (COSY)* with artifact-free PFG enhanced double-quantum-

544 filter[30] was performed. The second dimension was constructed by using 192 increments spanning

545 13 ppm. The relaxation delay was 2 s and the number of scans for each increment was 2.

546 *^{13}C distortionless enhancement polarization transfer (DEPT)* spectra were acquired with a shaped

547 pulse of 180° on ^{13}C, a 135° degree read pulse and proton decoupling were applied during

548 acquisition. The delay between the 90° and 180° pulses is 3.45 ms. This pulse sequence yields

549 positive peaks with one or three protons bonded to the carbon atom and negative peaks with two

550 protons bonded to the carbon atom.

551 *^{1}H/^{13}C correlation heteronuclear single quantum coherence (HSQC)* experiments were performed

552 via an insensitive nuclei enhanced by polarization transfer (INEPT) experiment[31-33]. Phase sensitive

553 acquisition with an echo/antiecho-TPPI gradient selection and decoupling was used during

554 acquisition. Trim pulses in for the INEPT transfer with multiplicity editing during the selection step

555 as well as shaped pulses for inversion on ^{13}C for matched sweep adiabatic pulses were also utilized

556 during acquisition. The second dimension (^{13}C) was constructed by 1024 increments spanning

557 190 ppm. The relaxation delay was 0.8 s and the number of scans for each increment was 4.

H-cell experiments in an Ar glovebox. *Study of electrolyte decomposition and battery self-discharge.* The solvent was prepared by dissolving 1 M KOH in D_2O followed by vigorous degassing for 2 hours and was loaded into a glovebox (oxygen level < 0.1 ppm), along with parts of the H-cell. The oxygen level of the solvent was measured to be 0 ppm (0.2 ppm accuracy) by a precision dissolved oxygen meter. 100 mM DHAQ and 300 mM $K_2Fe(CN)_6$ solutions were prepared in 20 cm^3 solvent and were placed in the H-cell inside the glovebox. The H-cell with a sampling port was made in-house (Supplementary Fig. 3a). Pretreated Nafion® membrane was sandwiched between the two half-cells. Three pieces of Sigracet carbon paper (39AA) with a dimension of 1 cm × 3 cm were immersed in the solution on each side and electrically connected to a portable Bio-Logic SAS (Model: SP-150). A charge current of 10 mA was applied to a cut-off voltage of 1.9 V and the voltage was continuously measured during cell resting for up to 470 hrs. The solution was stirred vigorously during the experiment. NMR, IR and MS analysis were performed on the solution and headspace gas during the charge-rest cycling.

Study of battery self-discharge by infrared spectroscopy. Attenuated total reflection (ATR) infrared spectra were acquired with a Cary 630 FTIR spectrometer inside an Ar glovebox. The spectral range was from 4000 to 400 cm^{-1} with a resolution of 2 cm^{-1}. 16 background and sample scans were performed.

During the charge and rest experiment, 10 mm^3 aliquots of DHAQ solution were extracted intermittently from the sampling port of the H-cell by a syringe. These were then dropped onto the spectrometer sampling window to enable IR spectra to be acquired.

Ex situ mass spectrometry (MS) was performed using an in-house system connected to a Pfeiffer ThermoStar™ quadrupole gas analysis system. The analysis was performed on 2 cm^3 gas sampled from the headspace of the same solution in the H-cell after the charge-rest cycling. 5 cm^3 syringes were used to extract the gas, and the syringes containing the sampled gas were transported in an air-tight plastic box from the glovebox to the MS. The transport time was approximately 2 minutes. The gas or solution was injected into an online T-shape glass sampler. The carrier gas was Ar at a flow rate of 100 μLn/s at 1.1 bar(a). The dwell time for m/z = 4 was 5 s.

Study of gas evolution by *in situ* MS. An electrochemical H-cell was designed and was connected to an online electrochemical mass spectrometry (OEMS) system (Supplementary Fig. 4a,b). The cell was based on two 1/2" stainless steel tees (Swagelok) interconnected via a liquid-tight glass union with a membrane fitted in the middle (Nafion® 212). Both sides of the cell were capped at the bottom with a round bottom glass test tube fitted with a magnetic stirrer and at the top with a stainless-steel plunger where a working electrode was affixed. All connections were made both liquid- and gas-tight with PTFE ferrules. The total internal volume of each compartment was ~10 cm^3. To sample the headspace (~1 cm^3) the top plunger of the anolyte (anthraquinone) compartment of the cell was fitted with two 1/16" tubes, that were connected to a gas line through double shut off quick connects (Beswick). The carrier gas (argon) flow was controlled by a mass flow controller and a pressure controller (Bronkhorst) and set to 200 μLn/s at 1.1 bar(a). After passing through the head space of the anolyte, the sample gas was fed to a quadrupole mass spectrometer (Pfeiffer Omnistar) through a capillary (ID = 0.22 mm) heated to 120 °C to prevent condensation. A potentiostat (Ivium Vertex) was connected to both sides of the cell to control the electrochemical operations.

Cyclic voltammetry. Electrochemical measurements were performed on a Biologic potentiostat (SP-150) using an in-house small-volume cyclic voltammetry cell. Polished 3 mm diameter glassy carbon (Biologic A-012744) was used as the working electrode while coiled platinum wire was used as the counter-electrode. For the reference, a mercury/mercury oxide (1 M KOH) electrode which has a potential of 0.14 V against standard hydrogen evolution (SHE) was used. The 1 M KOH solution was made under inert atmosphere by the addition of de-gassed Millipore water to a known quantity of potassium hydroxide. DHAQ (16 mg) or DBEAQ (41.2 mg) were dissolved in the KOH solution

606   (13.32 cm^3 and 10 cm^3 1 M KOH, respectively) under inert atmosphere. A sample of the solution
607   was then extracted and added to the nitrogen flushed small-volume electrochemical cell under inert
608   atmosphere. The electrodes were then checked to ensure that no bubbles had formed during the
609   addition of water before cycling was initiated. A constant overpressure of nitrogen was maintained
610   during the experiment. The voltage was scanned from 0 V to -1.5 V at 20 mV/s.

611   **Equilibrium concentrations of DHAQ^{2-}, DHAQ$^{3-\bullet}$ and DHAQ^{4-}, and CV fittings.** In Extended
612   Data Fig. 4h, we have fitted the first full CV cycle with four different approaches. The two 2e$^-$
613   processes are for an illustrative comparison, while the third and fourth (both 1e$^-$ + 1e$^-$) are more
614   relevant. In each case, we implemented code using the SciPy library and its curve fitting function. As
615   the values that were to be fitted have differing orders of magnitude, the x_scale = 'jac' option was
616   used to rescale variables to aid in the fits. The diffusion coefficients were assumed to be the same for
617   each species and where relevant, the electron transfer rate. The symmetry factor α was set to 0.5. For
618   approach four, diffusion coefficients and electron transfer rates were not constrained to be the same
619   for all species. Initial guesses for the fits were set to be in line with the reported experimental data.

620   For approach three, the fitted voltage difference was averaged over the 68 cycles analysed here and
621   found to be 60 mV. This is in line with previously reported data[5]. However, these values are twice
622   what we found from our comproportionation calculations coupled with the Evans' method. The
623   average diffusion coefficient is 2.7×10^{-10} m^2/s. The average potentials (vs Hg/HgO (1M KOH)) were
624   -0.804 V and -0.864 V. The k_0 values had a far larger distribution in our fits, as the average of 3×10^{-3}
625   cm/s had a standard deviation of 2×10^{-3} - 3×10^{-3} cm/s.

626   Approach four gave a fitted voltage difference of 30 mV, which matches very well with the 33 mV
627   value derived from the Evans' method. The other fitted parameters are as follows: diffusion
628   coefficients were 3.0×10^{-10}, 1.0×10^{-10} and 7.8×10^{-10} m^2/s for DHAQ^{2-}, DHAQ$^{3-\bullet}$ and DHAQ^{4-},
629   respectively. The potentials were E_1 = -0.800 V and E_2 = -0.830 V. $k_{0,1}$ and $k_{0,2}$ converged to the
630   same value, 7×10^{-3} cm/s .

631   These approaches (Extended Data Fig. 4h) show that the redox reactions are far more likely to be
632   two one-electron steps rather than a single two-electron step. To get the voltage difference, E_1-E_2, is
633   non-trivial and inconsistent results are returned due to the complexity of the fitting procedure. Such
634   non-linear least squares fitting can be very sensitive to initial conditions and constraints used.
635   Comparing these approaches with the comparative simplicity of utilising the equilibrium constant
636   along with the Evans' method shows that for E_1-E_2 all the fits are reasonable. We believe that the
637   Evans' method provides an independent method for determining E_1-E_2, that, at least in the DHAQ
638   case, is associated with smaller errors (i.e. is more accurate) than the values provided purely through
639   fitting of the CV data.

640   The current model does not capture the asymmetry in the HOD shift as a function of SOC, which
641   leads to an asymmetry in the calculated DBEAQ$^{3-\bullet}$ radical concentrations as a function of SOC
642   (Extended Data Fig. 4d). This suggests that either a competing reaction is present that depletes the
643   radical concentration at higher concentrations of DBEAQ^{4-} or possibly that changes in the solvation
644   of the ions with SOC also lead to changes in the HOD chemical shift.

645   **EPR experiment.** The X-band EPR experiment was performed on a solution of 100 mM and 1 mM
646   DHAQ, reduced to approximately 50% SOC, respectively, using a Bruker EMX spectrometer. For
647   the 100 mM DHAQ, the field was swept from 3000 to 4000 Gauss. The microwave frequency was
648   9.865410 GHz. For the 1 mM DHAQ sample, the field was swept from 3463 to 3563 Gauss. The
649   microwave frequency was 9.865408 GHz. The attenuation was 20 dB, the amplitude of modulation
650   is 0.1 Gauss, the power was 2 mW, and the sweep time is 20 s for both experiments. A Bruker
651   AquaX sampling tube (30 mm^3/cm) was used for data acquisition.

652 EasySpin was used to fit the spectra[34]. Spin systems of one unpaired electron coupled to

653 different numbers of proton and deuterium spins were set up, taking into account the H-D

654 exchange in deuterated solvent D_2O. For the non-deuterated $DHAQ^{3-\bullet}$, a spin system of three

655 protons with two magnetically equivalent spins for each proton was modelled. For singly

656 deuterated $DHAQ^{3-\bullet}$, a spin system of two protons with two magnetically equivalent spins for

657 each proton, another proton with a single spin and a deuteron with a single spin was set up. For

658 the doubly deuterated $DHAQ^{3-\bullet}$, a spin system of two protons with two magnetically equivalent

659 spins for each proton and one deuteron with two magnetically equivalent spins was set up. The

660 fitted variables were g-factors, hyperfine coupling constants, the fractions of each component,

661 and linewidth. The method of Nelder/Mead simplex was used. The fitted EPR spectra using a

662 single component of non-deuterated $DHAQ^{3-\bullet}$, two components of non-deuterated and singly

663 deuterated $DHAQ^{3-\bullet}$, and two components of non-deuterated and doubly deuterated $DHAQ^{3-\bullet}$,

664 respectively are presented in Extended Data Fig. 3b-d. The two component system comprising

665 non-deuterated (92.6%) and doubly deuterated (7.4%) $DHAQ^{3-\bullet}$ gives the lowest root mean

666 square deviation (rmsd) of 0.0175. The fit yields a g-factor of 2.0077 and hyperfine coupling

667 constants of 0.15 MHz, 2.63 MHz and 4.64 MHz for each unique proton. The other two fits yield

668 similar results. The difference between the g-factors of the 100 mM (2.0036) and 1 mM solution

669 (2.0077) is possibly due to motional effects from the varying viscosity of the solution or the

670 magnetic field drift of the instrument.

671 To understand the effect of the hyperfine coupling on the NMR chemical shift, we need to correlate

672 the paramagnetic component of the shift δ to the isotropic (Fermi-contact) hyperfine coupling

673 constant (A_{iso}). By definition, A_{iso} describes the strength of the electron-nuclear spin coupling (*i.e.*

674 the unpaired spin density at the nucleus) in the limit of *static* (non-flipping) electronic spins. At finite

675 temperatures, however, the paramagnetic behaviour of the electrons means that they undergo a rapid

676 flipping between the two spin states of a spin-1/2 system. In an EPR experiment where the electronic

677 spin transitions are observed on the timescale of ps to ns, this results in a coupling which is

678 evidenced (at least in the dilute system) by splitting of the resonance by A_{iso}. In NMR experiments,

679 however, the much longer timeframe of the nuclear spin transitions (~μs) effectively decouples the

680 electronic transitions from the nuclear transitions. The net effect of this that only the time-averaged

681 electronic spin moment is felt by the nuclear spin, and the strength of this effective coupling

682 determines the observed Fermi-contact NMR shift. This scaling is typically done by means of the

683 magnetic susceptibility χ, which for a Curie-Weiss system, depends inversely on the temperature T.

684 The isotropic component of the total shift δ_{iso} can then be written as a sum of the diamagnetic

685 (chemical shift) and paramagnetic (Fermi-contact) components: $\delta_{iso} = \delta_{CS} + \delta_{FC}$. The temperature

686 dependence of δ_{FC} is expressed as (in ppm),

687
$$\delta_{FC} = A_{iso}\left(\frac{\gamma_e}{\gamma_H}\right)\left(\frac{h}{4k_BT}\right)\cdot 10^6 \qquad [3]$$

688 where γ_e (γ_H) is the electron (proton) gyromagnetic ratio, h is the Planck constant, and k_B is the

689 Boltzmann constant. The expected shifts determined from the DFT calculations and via EPR

690 (Extended Data Fig. 3e) are shown along with A_{iso} for the $DHAQ^{3-\bullet}$ radical and the corresponding

691 EPR data.

692 While the EPR investigation of this redox system is still ongoing and subject to a separate

693 study, the preliminary results clearly show why the ${}^1H$ NMR shift of proton *b* on reduction is

694 relatively small. The disappearance of the ${}^1H$ NMR resonances of protons *a* and *c* on reduction is

695 ascribed to the much larger hyperfine shifts associated with these protons (see Fig. 3d in the main

696 text). We have not accounted for any pseudocontact contributions to the NMR shifts, because the

697 effective g-factor is very close to the free-electron value, suggesting that they are extremely
698 small.

699 **Application considerations in RFBs and beyond.** Organic RFBs based on inexpensive (the
700 estimated price of, for example, anthraquinone disulfonic acid is currently in the range of US$0.9/kg
701 to US$3.9/kg for industrial-scale production[35]) and sustainable redox-active materials are promising
702 storage technologies, which are cheaper and have fewer environmental hazards as compared to the
703 more established and mature vanadium-based (the price of vanadium pentoxide in Europe is in the
704 range of US$19.4/kg – US$63.5/kg in 2018[36]).
705   Because of the simplicity of the *on-line* NMR setup, which consists essentially of a lab-scale RFB
706 and a flow NMR sampling tube, we expect wide adoption of this technique to advance the
707 understanding of a variety of redox chemistry, such as quinone-[37,38], carbonyl-nitrogen-[39], radical-[40],
708 polymer-[41], and metal complex-[42] based redox chemistries in flow and other battery systems,[3-5,39,43-52]
709 e.g. lithium-air batteries that involve organic redox shuttles. This technique can be readily coupled
710 with other (flow) characterizations, including in situ mass spectrometry, EPR and optical methods. In
711 addition to the study of redox chemistry, the on-line technique can be exploited to study the rate of
712 electrolyte crossover, which would help improve membrane design. The operando design lays the
713 foundation for future magnetic resonance imaging experiments to monitor flow, and the
714 electrolyte/solvent distribution in the electrode.
715   The Evans' method allows the radical concentration to be determined from the magnetic
716 susceptibility. This affords a straightforward approach to track the SOC of the anolyte and catholyte,
717 providing critical information about cell balancing, and how that varies with cycle life. This is not
718 easy information to determine from full cell measurements without the use of a reference electrode.
719 Of note, our results also motivate the development of simpler and cheaper methods to extract this
720 information by using a magnetometer or a relaxometer. It is foreseeable that the *in situ* NMR and
721 related metrologies will contribute to both the fundamental and practical understanding, and the
722 development of longer-lasting and flow batteries with higher energy densities for large-scale energy
723 storage in the near future.

725 **Data availability.** The data that support the findings of this study are available from
726 www.repository.cam.ac.uk and the corresponding author upon reasonable request.

728 27.   Dalitz, F., Cudaj, M., Maiwald, M. & Guthausen, G. Process and reaction monitoring by low-field NMR
729   spectroscopy. *Prog. Nucl. Magn. Reson. Spectrosc.* **60**, 52-70 (2012).
730 28.   Hogben, H. J., Krzystyniak, M., Charnock, G. T. P., Hore, P. J. & Kuprov, I. Spinach – A software library for
731   simulation of spin dynamics in large spin systems. *J. Mag. Reson.* **208**, 179-194 (2011).
732 29.   Johnson Jr., C. S. Diffusion ordered nuclear magnetic resonance spectroscopy: principles and applications.
733   *Prog. Nucl. Magn. Reson. Spectrosc.* **34**, 203-256 (1999).
734 30.   Shaw, A. A., Salaun, C., Dauphin, J.-F. & Ancian, B. Artifact-free PFG-enhanced double-quantum-filtered
735   COSY experiments. *J. Mag. Reson., Series A* **120**, 110-115 (1996).
736 31.   Willker, W., Leibfritz, D., Kerssebaum, R. & Bermel, W. Gradient selection in inverse heteronuclear correlation
737   spectroscopy. *Magn. Reson. Chem.* **31**, 287-292 (1993).
738 32.   Zwahlen, C. *et al.* Methods for measurement of intermolecular NOEs by multinuclear NMR spectroscopy:
739   application to a bacteriophage λ N-Peptide/boxB RNA complex. *J. Am. Chem. Soc.* **119**, 6711-6721 (1997).
740 33.   Boyer, R. D., Johnson, R. & Krishnamurthy, K. Compensation of refocusing inefficiency with synchronized
741   inversion sweep (CRISIS) in multiplicity-edited HSQC. *J. Mag. Reson.* **165**, 253-259 (2003).
742 34.   Stoll, S. & Schweiger, A. EasySpin, a comprehensive software package for spectral simulation and analysis in
743   EPR. *J. Mag. Reson.* **178**, 42-55 (2006).
744 35.   Vincent, D. *et al.* Estimating the cost of organic battery active materials: a case study on anthraquinone
745   disulfonic acid. *Transl. Mater. Res.* **5**, 034001 (2018).
746 36.   *vanadiumprice.com*.
747 37.   Yang, Z. *et al.* Alkaline benzoquinone aqueous flow battery for large-scale storage of electrical energy. *Adv.
748   Energy Mater.* **8**, 1702056 (2018).

749 38. Gerhardt, M. R. *et al.* Anthraquinone derivatives in aqueous flow batteries. *Adv. Energy Mater.* **7**, 1601488
750 (2017).
751 39. Orita, A., Verde, M. G., Sakai, M. & Meng, Y. S. A biomimetic redox flow battery based on flavin
752 mononucleotide. *Nat. Commun.* **7**, 13230 (2016).
753 40. Wei, X. *et al.* TEMPO-based catholyte for high-energy density nonaqueous redox flow batteries. *Adv. Mater.*
754 **26**, 7649-7653 (2014).
755 41. Janoschka, T. *et al.* An aqueous, polymer-based redox-flow battery using non-corrosive, safe, and low-cost
756 materials. *Nature* **527**, 78-81 (2015).
757 42. Chen, J.-J., Symes, M. D. & Cronin, L. Highly reduced and protonated aqueous solutions of $[P_2W_{18}O_{62}]^{6-}$ for
758 on-demand hydrogen generation and energy storage. *Nat. Chem.* **10**, 1042-1047 (2018).
759 43. Winsberg, J., Hagemann, T., Janoschka, T., Hager, M. D. & Schubert, U. S. Redox-flow batteries: from metals
760 to organic redox-active materials. *Angew. Chem. Int. Ed.* **56**, 686-711 (2017).
761 44. Kowalski, J. A., Su, L., Milshtein, J. D. & Brushett, F. R. Recent advances in molecular engineering of redox
762 active organic molecules for nonaqueous flow batteries. *Current Opinion in Chemical Engineering* **13**, 45-52
763 (2016).
764 45. Kwon, G. *et al.* Multi-redox molecule for high-energy redox flow batteries. *Joule* **2**, 1771-1782 (2018).
765 46. DeBruler, C. *et al.* Designer two-electron storage viologen anolyte materials for neutral aqueous organic redox
766 flow batteries. *Chem* **3**, 961-978 (2017).
767 47. Service, R. F. Advances in flow batteries promise cheap backup power. *Science* **362**, 508-509 (2018).
768 48. Ji, Y. *et al.* A phosphonate-functionalized quinone redox flow battery at near-neutral pH with record capacity
769 retention rate. *Adv. Energy Mater.*, 1900039 (2019).
770 49. Huskinson, B. *et al.* A metal-free organic–inorganic aqueous flow battery. *Nature* **505**, 195 (2014).
771 50. Ding, Y., Zhang, C., Zhang, L., Zhou, Y. & Yu, G. Molecular engineering of organic electroactive materials for
772 redox flow batteries. *Chem. Soc. Rev.* **47**, 69-103 (2018).
773 51. Holland-Cunz, M. V., Cording, F., Friedl, J. & Stimming, U. Redox flow batteries - concepts and chemistries
774 for cost-effective energy storage. *Front. Energy* **12**, 198-224 (2018).
775 52. Ding, Y., Li, Y. & Yu, G. Exploring Bio-inspired Quinone-Based Organic Redox Flow Batteries: A Combined
776 Experimental and Computational Study. *Chem* **1**, 790-801 (2016).
777 53. Ross, R. T. Dipolar broadening of EPR spectra due to solute segregation in frozen aqueous solutions. *J. Chem.*
778 *Phys.* **42**, 3919-3922 (1965).

792 **Author contributions**: C.P.G. supervised the project. E.W.Z and C.P.G. conceived the idea. E.W.Z.
793 designed the *in situ* setups, performed the NMR and EPR experiments and analysis with assistance
794 from H. S. T.L. and E.W.Z. performed the IR experiments. E.J. performed the calculations of
795 reaction equilibrium, CV fittings and NMR chemical shift. J. L. performed the DFT calculations of
796 SOMO. I.T. and E.W.Z. designed and performed the *in situ* mass spectrometry with assistance from
797 T.L. R.J. performed the CV experiments. A. W. synthesized DBEAQ under the supervision of Q. S.
798 All authors contributed to the discussion of the project. E.W.Z. and C.P.G. wrote the manuscript with
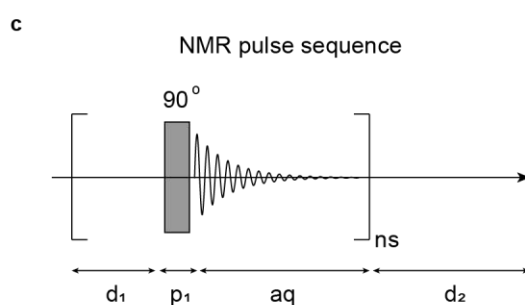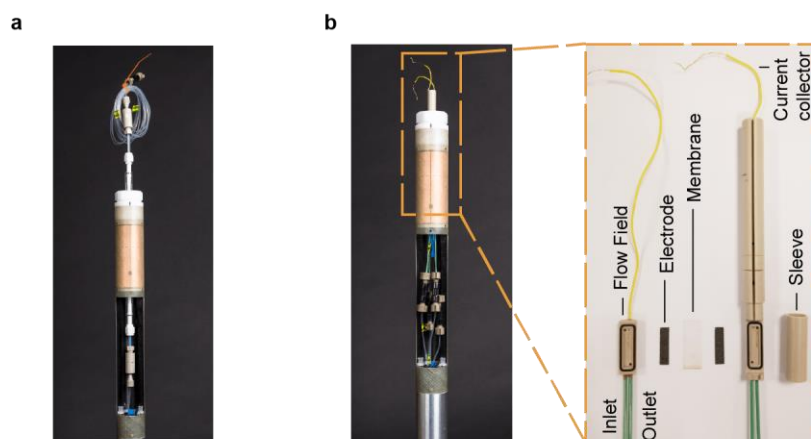799 input from all co-authors.
800 **Competing interests** The authors declare no competing interests
801
802 **Additional information**
803 **Extended data** is available for this paper at.

Rotary speed (rpm)	60	80	100	120	140	160	200
Flow rate (cm³/min)	13.6	17.7	22.2	27.3	30.0	33.3	37.5

Extended Data Fig. 1 | The *in situ* NMR probe setups and pulse sequence. a, Image of the flow-through (*on-line*) sampling tube positioned inside a Bruker 2.5 micro-imaging probe. **b**, The *operando* cell assembly positioned inside the NMR probe. The image on the right shows the components of the cell assembly. **c**, Each spectrum is acquired by collecting *ns* free induction decays (FIDs; i.e., scans) with a recycle delay in between, d_1. A second time delay, d_2 is introduced between each spectrum. The pulse width, p_1, for a 90° pulse is 27 μs. The acquisition time for each FID, aq, is 1.5 s. **d**, Measured flow rates as a function of rotary speed of the pump.
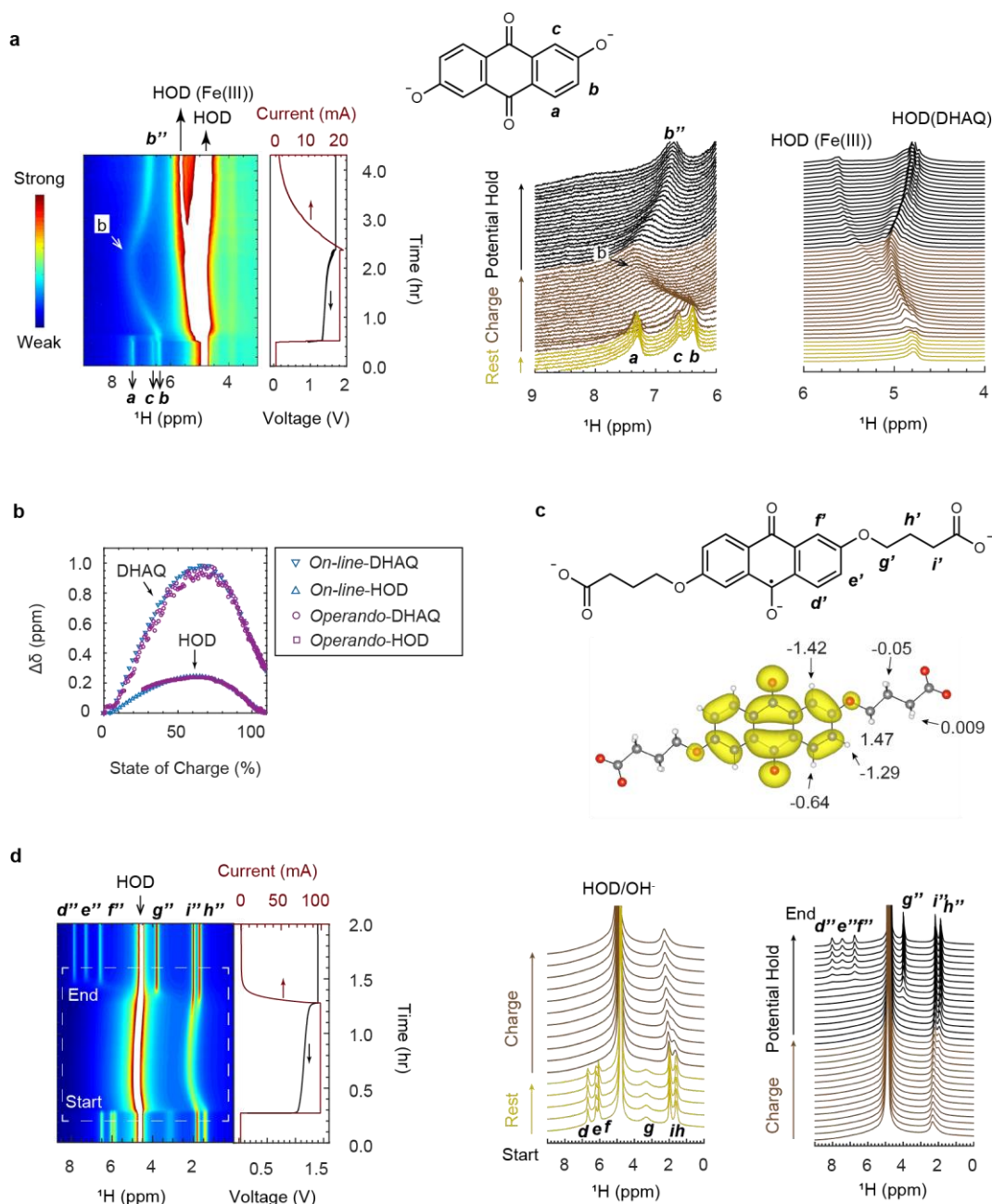
Extended Data Fig. 2 | The *in situ* pseudo-2D and stacked ^{1}H NMR spectra versus battery voltage and current. a, *Operando* NMR spectra of 10 cm^3 100 mM DBEAQ, against 20 cm^3 150 mM potassium ferrocyanide. The FWHM of the water signal acquired via *on-line* detection is 6 Hz, compared to the FWHM of 59 Hz acquired in the *operando* setup. b, Shift of the DHAQ-H^b and water resonances as a function of state of charge measured via *on-line* and *operando* detection. The shifts of the water resonances were only included in the plot after there is clear peak separation between the water signals arising fro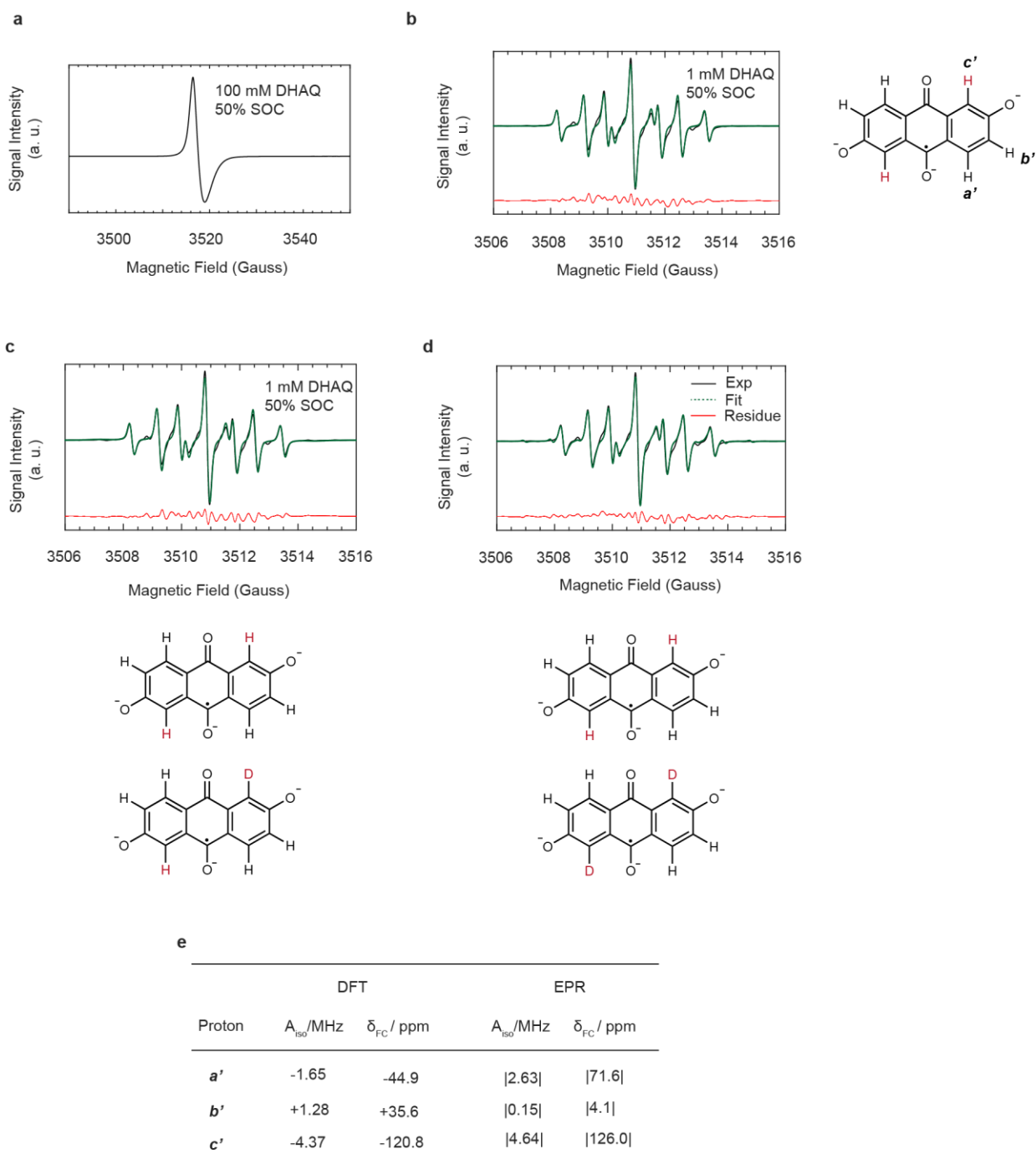m the catholyte and anolyte electrolytes. c, Labeling of the protons, DFT derived volumetric plots of the SOMO for DBEAQ$^{3-•}$. d, *On-line* NMR spectra of 20 cm^3 100 mM DBEAQ (anolyte), against 20 cm^3 300 mM potassium ferrocyanide (catholyte).

a

100 mM DHAQ
50% SOC

Signal Intensity (a. u.)

Magnetic Field (Gauss)
3500 3520 3540

b

1 mM DHAQ
50% SOC

Signal Intensity (a. u.)

Magnetic Field (Gauss)
3506 3508 3510 3512 3514 3516

c

1 mM DHAQ
50% SOC

Signal Intensity (a. u.)

Magnetic Field (Gauss)
3506 3508 3510 3512 3514 3516

d

— Exp
...... Fit
— Residue

Signal Intensity (a. u.)

Magnetic Field (Gauss)
3506 3508 3510 3512 3514 3516

e

Proton	DFT		EPR	
	A_{iso}/MHz	δ_{FC}/ ppm	A_{iso}/MHz	δ_{FC}/ ppm
a'	-1.65	-44.9	|2.63|	|71.6|
b'	+1.28	+35.6	|0.15|	|4.1|
c'	-4.37	-120.8	|4.64|	|126.0|

Extended Data Fig. 3 | EPR spectra of DHAQ$^{3-\bullet}$ radical anions. a-d, Spectra of 100 mM, 1 mM DHAQ solution reduced to 50% SOC, fitted with a single component comprising of non-deuterated DHAQ$^{3-\bullet}$, two components comprising of non-deuterated and singly deuterated DHAQ$^{3-\bullet}$, and two components comprising of non-deuterated and doubly deuterated DHAQ$^{3-\bullet}$, respectively. At 100 mM, an intense EPR signal of DHAQ$^{3-\bullet}$ was observed at 3518 Gauss (g = 2.0036). However, the signal is significantly broadened by a combination of the electron dipolar interactions at such a high radical concentrations and the rapid electron transfer reactions. This leads to the loss of the hyperfine coupling features[53]. At 1 mM, hyperfine coupling features were resolved. **e**, Table showing DFT and EPR-derived isotropic hyperfine coupling constants (A_{iso}) and contact shifts of the proton resonances. The source of the difference between the DFT and EPR-derived hyperfine coupling constants is likely due to solvent (water) coordination, H-D exchange, and/or electron hopping.
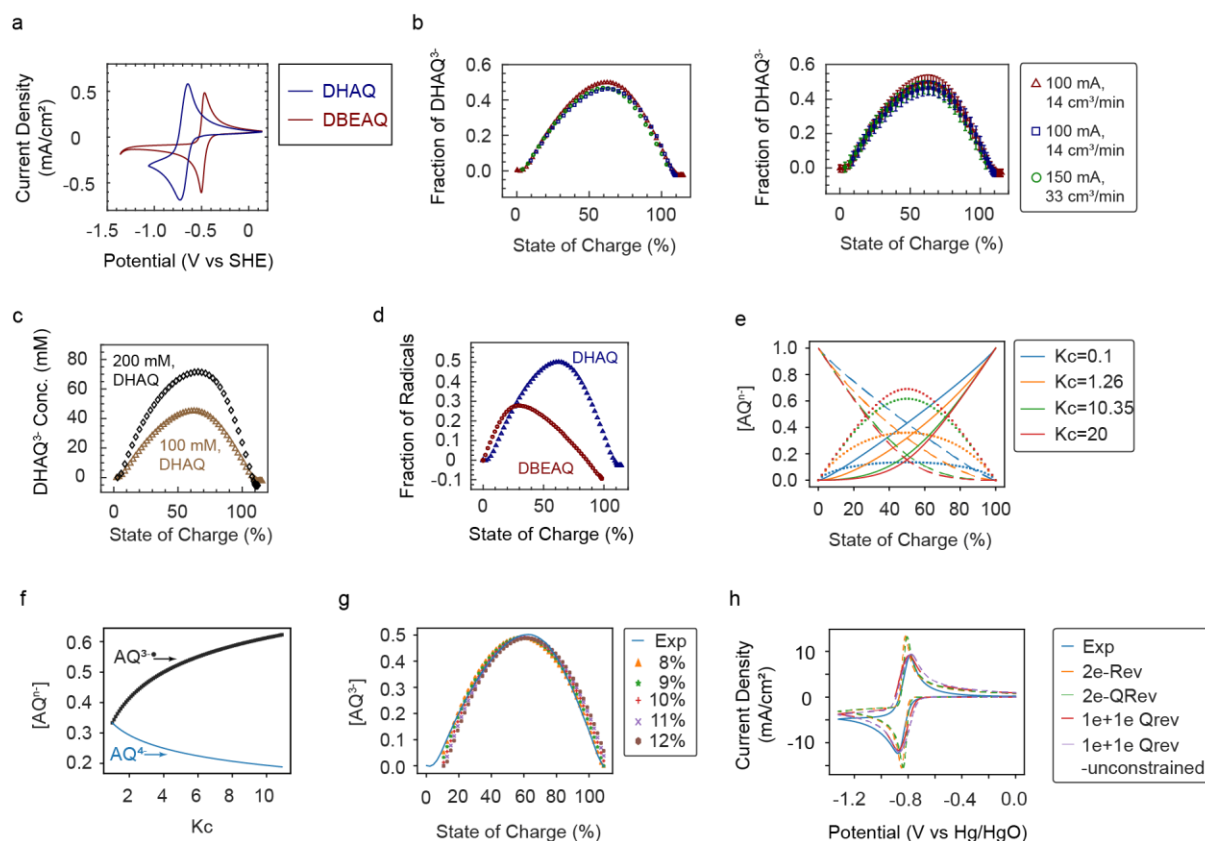
23

Extended Data Fig. 4 | CV and concentration of radical anions. a, CV of 5 mM DHAQ and 5 mM DBEAQ in D_2O with 1 M KOH. The potential was scanned at 20 mV/s from positive to negative potential. **b**, Fraction of $DHAQ^{3-\bullet}$ radicals calculated based on the Evans' method as a function of SOC for DHAQ (100 mM) under a charging current of 100 mA and a flow rate of 13.6 cm^3/min (measured twice), and a charging current of 150 mA and a flow rate of 33.3 cm^3/min. The figures on the right and left are the same data plotted without and with error bars. The errors were calculated using the FWHM of the water signal. **c, d**, Fraction of $DHAQ^{3-\bullet}$ radicals as a function of SOC for 100 mM, 200 mM DHAQ and 100 mM DBEAQ. **e**, Relative concentrations of AQ^{2-}, $AQ^{3-\bullet}$ and AQ^{4-} as a function of state of charge of the system and equilibrium constant, K_c. AQ^{2-}, $AQ^{3-\bullet}$ and AQ^{4-} are represented by dashed, dotted and solid lines, respectively. $K_c = 1.26$ and $K_c = 10.35$ correspond to values derived for DBEAQ and DHAQ, respectively (corresponding to E_1-E_2 values of 6 and 60 mV, respectively from obtained in the literature[5,13]). Curves corresponding to $K_c = 0.1$ and $K_c = 20$ are also shown to illustrate the effect using smaller and higher E_1-E_2 values of -58.3 and 76.6 mV, respectively, the former negative value illustrating the case where the radical is strongly disfavoured. **f**, The $AQ^{3-\bullet}$ and AQ^{4-} concentration at 50% SOC, as a function of K_c. $AQ^{3-\bullet}$ and AQ^{4-} are dotted and solid lines, respectively. **g**, Experimentally derived radical concentrations as a function of state of charge. Equations S6 and S7 were used to fit the experimental data along with a state of charge lag parameter (discussed along with the derivation of the equations in the SI), ranging from 8% to 12%, where x is the fraction of $AQ^{3-\bullet}$ for a given number of electrons, n. Data were calculated in SOC steps of 1%. **h**, The CV of a 100 mM DHAQ; 2e-Rev and 2e-QRev refer to a two electron, reversible and quasi-reversible model respectively and the 1e+1e curves refer to a two-step, one-electron quasi-reversible process.
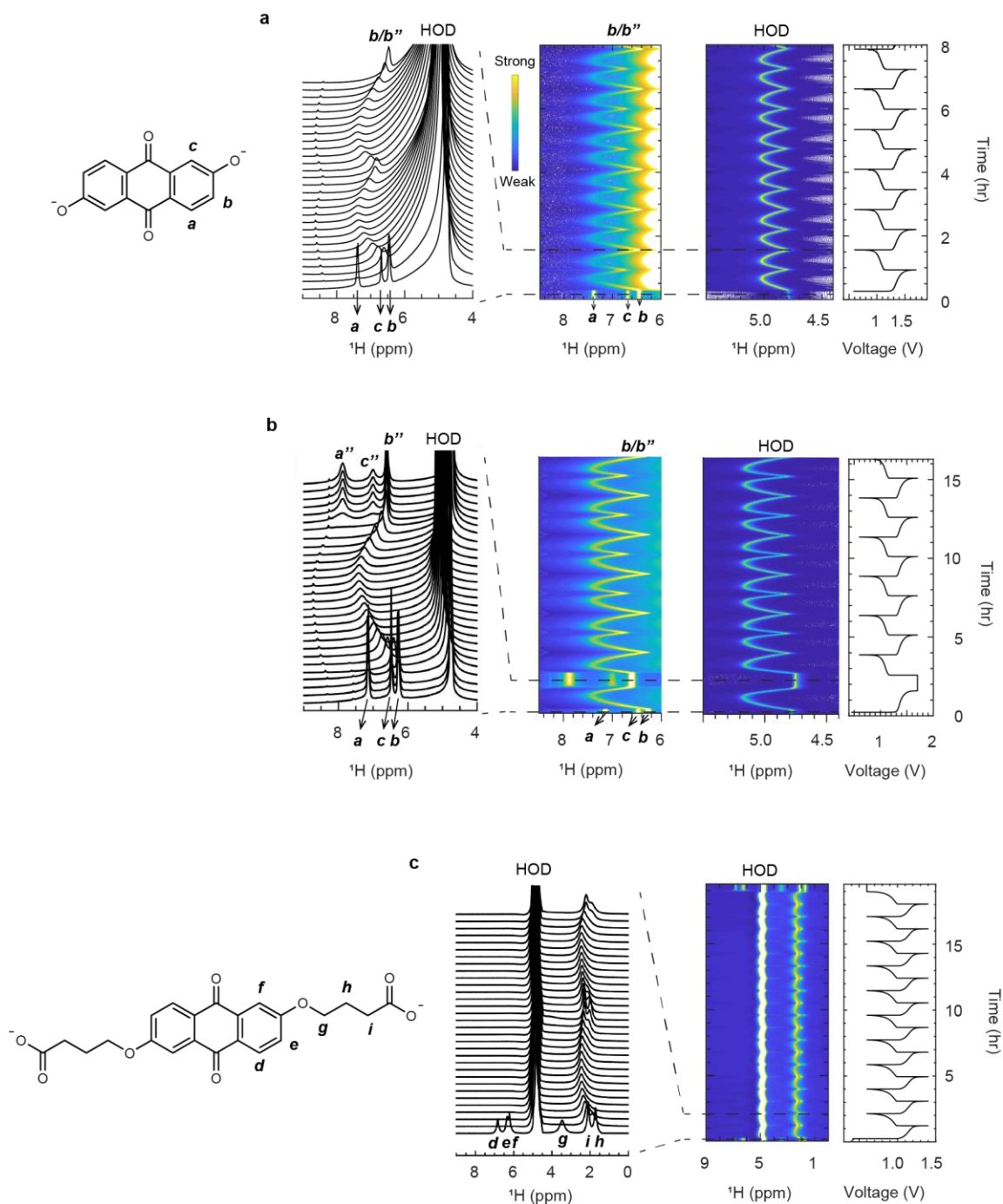
866
Extended Data Fig. 5 | *On-line* ^{1}H NMR spectra and battery electrochemical profile during
galvanostatic cycling. a, 20 cm^3 100 mM DHAQ against 40 cm^3 150 mM ferrocyanide/50 mM
ferricyanide. The flow rate is 33.3 cm^3/min and the current is 150 mA. With a recycle delay of 20 s,
an acquisition time of 1.5 s and 4 scans, each spectrum is a snapshot of the electrochemical processes
averaged over 2.5% of the SOC. **b**, 20 cm^3 200 mM DHAQ against 40 cm^3 250 mM ferrocyanide/
50 mM ferricyanide. The flow rate is 13.6 cm^3/min and the current is 150 mA. With a recycle delay
of 15 s, an acquisition time of 1.5 s and 8 scans, each spectrum is a snapshot of the electrochemical
processes averaged over 2.9% of the SOC. **c**, 20 cm^3 100 mM DBEAQ against 40 cm^3 150 mM
ferrocyanide/50 mM ferricyanide. The flow rate is 13.6 cm^3/min and the current is 100 mA. With a
recycle delay of 7 s, an acquisition time of 1.5 s and 8 scans, each spectrum is a snapshot of the
electrochemical processes averaged over 2.1% of the SOC.
878

25
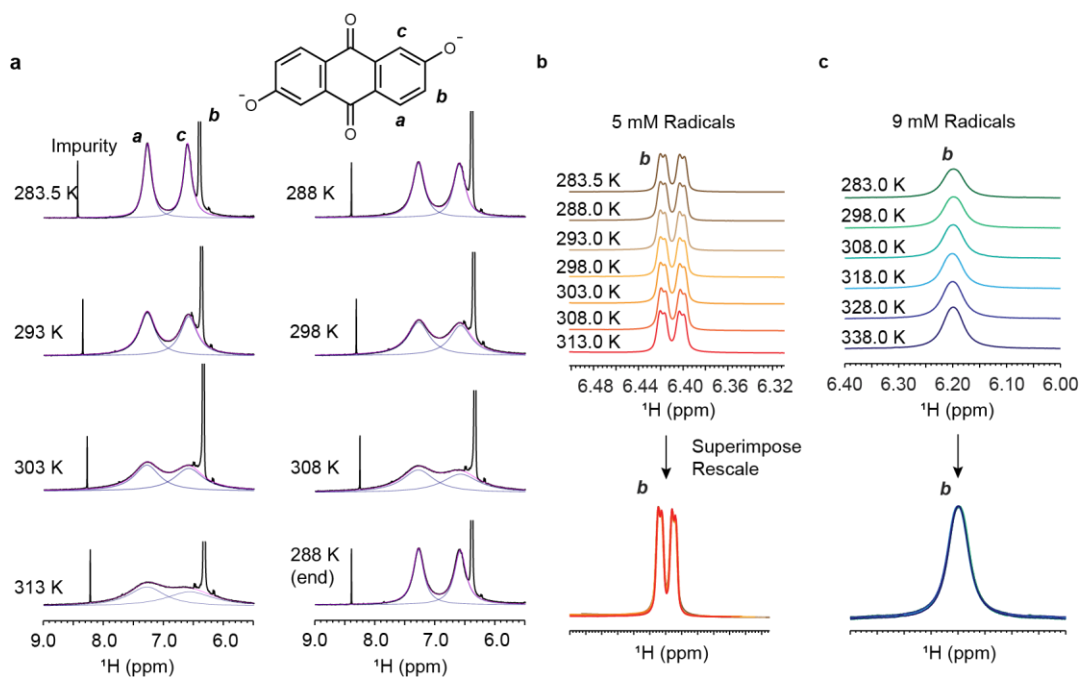
Extended Data Fig. 6 | Variable temperature NMR of DHAQ^{2-}/DHAQ$^{3-\bullet}$ radical anion solution.
a, VT NMR spectra acquired from a solution containing 5 mM radicals in 100 mM DHAQ. Black: experimental spectra; Navy: deconvoluted spectra; Magenta: fitted sum spectra. VT NMR spectra of peak **b** with 5 mM (**b**) and 9 mM (**c**) radicals, respectively. As the experiments were performed by locking the magnetic field on the shift of the water resonance, which is temperature-dependent, the shift of peak **a** was manually set to 7.3 ppm so as to compare the different spectra more readily.
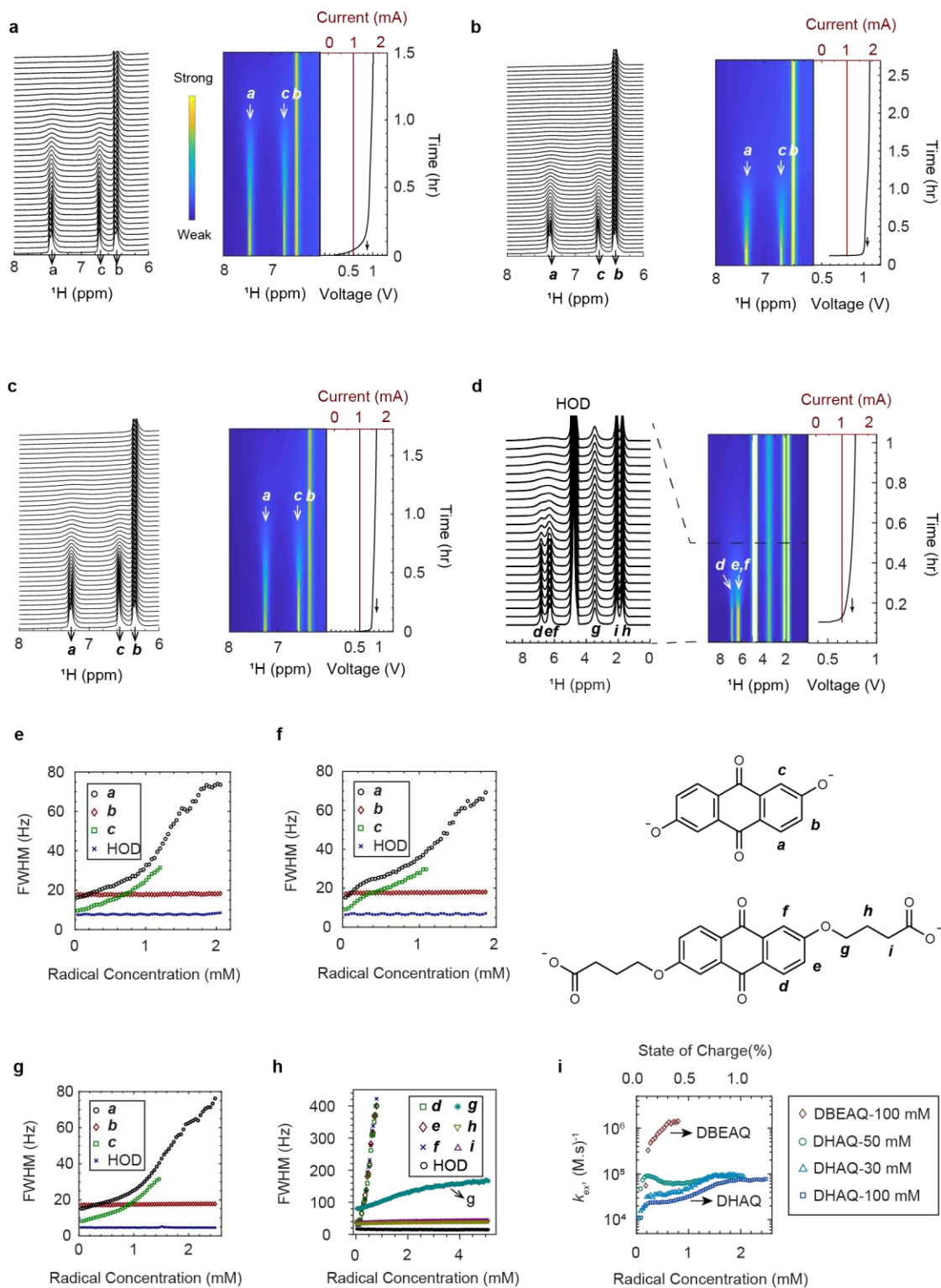
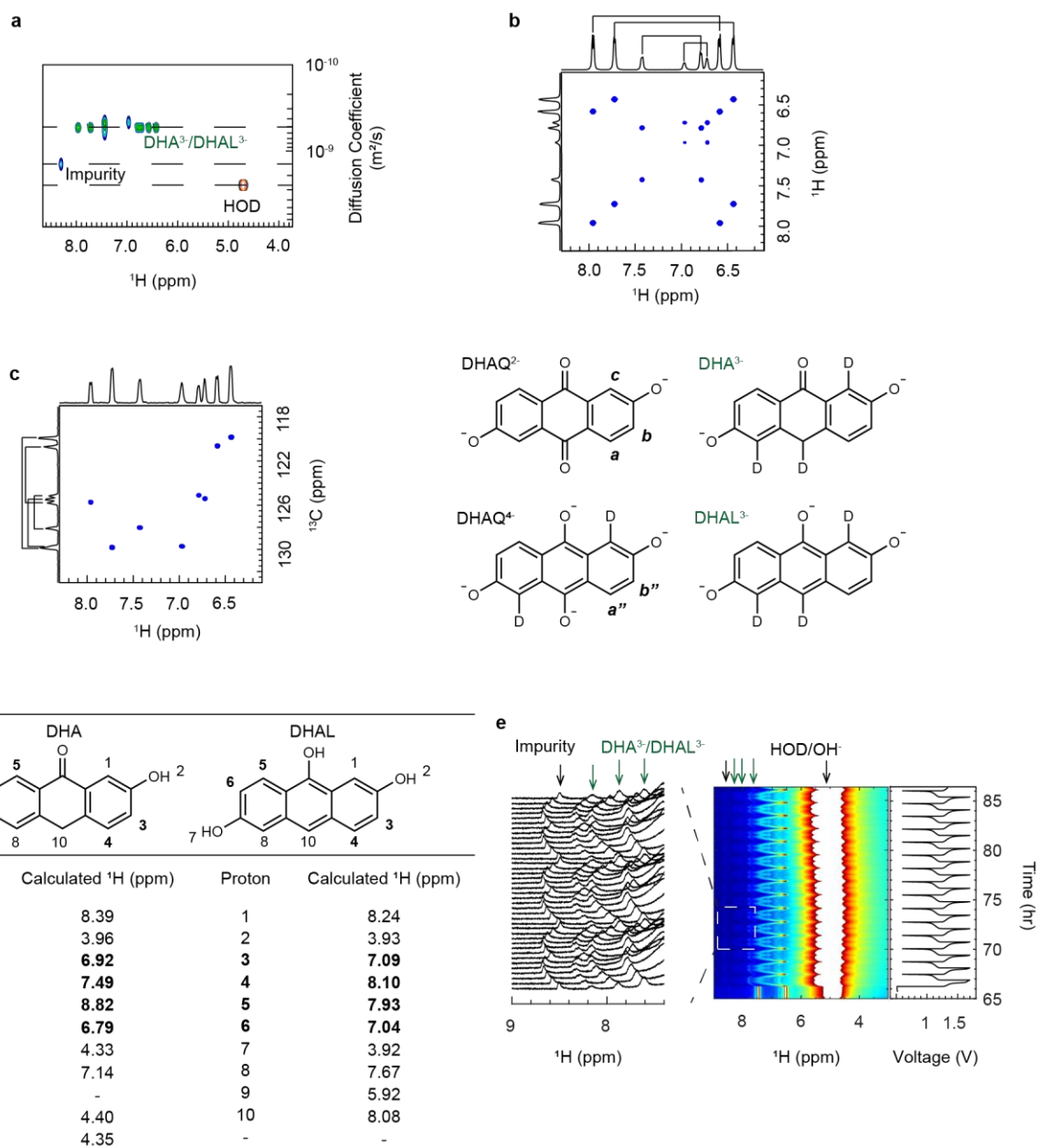**Extended Data Fig. 7 | *On-line* ¹H NMR spectra performed to quantify the electron transfer rates. a**, 30 mM, **b**, 50 mM, **c**,100 mM 2,6-DHAQ and **d**,100 mM 2,6-DBEAQ during charge/reduction at 1 mA. **e-h**, The FWHM of the proton signal ***a***, ***b***, ***c*** of DHAQ and ***d-i*** of DBEAQ as a function of radical concentrations. **i**, The electron transfer rate constant k_{ex} calculated for 30, 50 and 100 mM DHAQ and 100 mM DBEAQ at different radical concentrations/SOC, under the slow-exchange approximation.

d, DHA / DHAL structures and table

Proton	Calculated ¹H (ppm)	Proton	Calculated ¹H (ppm)
1	8.39	1	8.24
2	3.96	2	3.93
3	**6.92**	**3**	**7.09**
4	**7.49**	**4**	**8.10**
5	**8.82**	**5**	**7.93**
6	**6.79**	**6**	**7.04**
7	4.33	7	3.92
8	7.14	8	7.67
-	-	9	5.92
10	4.40	10	8.08
10	4.35	-	-

894

895 **Extended Data Fig. 8 | NMR and DFT calculations to identify the decomposition products. a**,
896 DOSY, **b**, COSY, **c**, HSQC spectra of the aliquot extracted from the H-cell at 470 hours (see H-Cell
897 Experiments in Ar Glovebox in Methods section for details) in an air-tight NMR tube. The lines
898 above the COSY and HSQC spectra indicate the connectivity of the H and C atoms. **d**, DFT-derived
899 (calculated) proton chemical shift of DHA and DHAL. **e**, *In situ* NMR during the galvanostatic
900 cycling at 100 mA after the potential-hold (1.7 V) step. Green arrows: DHA³⁻/DHAL³⁻.

901
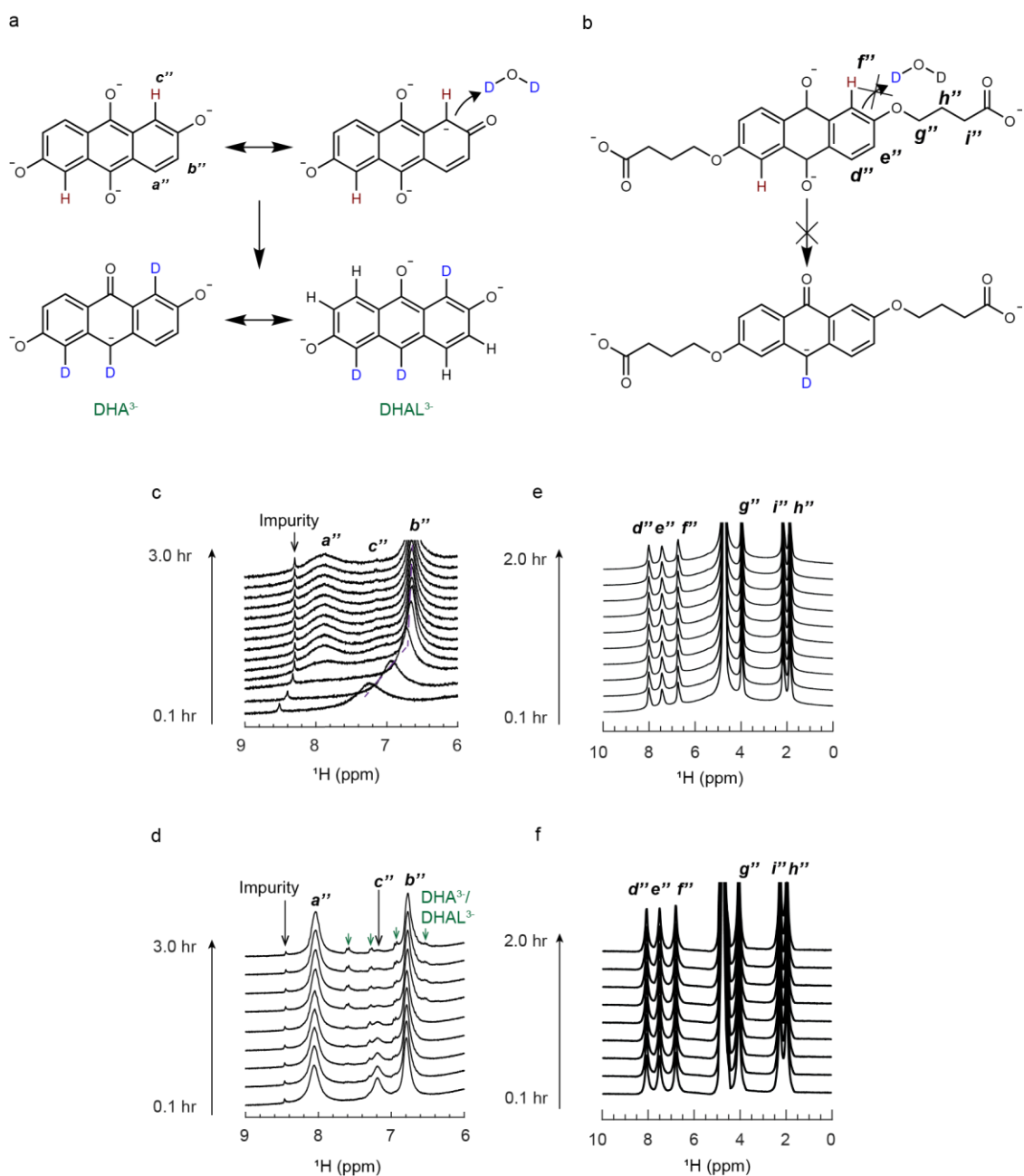
Extended Data Fig. 9 | *In situ* ^{1}H NMR study of the decomposition reaction under different cycling conditions. a, **b**, Proposed H-D exchange (top) and decomposition (bottom) reaction and products of DHAQ^{4-} and DBEAQ^{4-}, respectively. NMR spectra of DHAQ during potential hold at **c**, 1.4 V and **d**, 1.7 V. Green arrows: DHA^{3-}/DHAL^{3-}. NMR spectra of DBEAQ during potential hold at **e**, 1.4 V and **f**, 1.7 V.
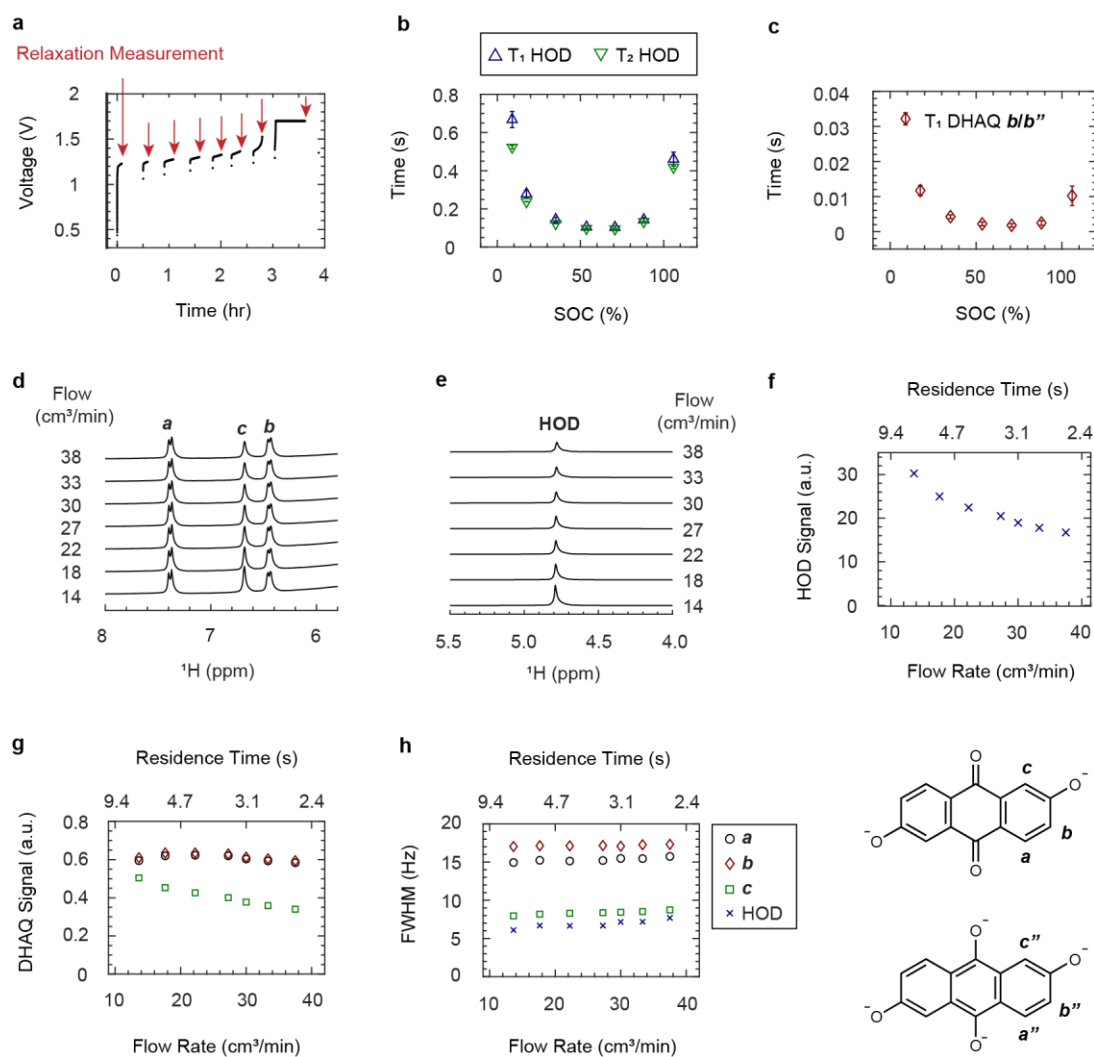
Extended Data Fig. 10 | Effect of radical and flow on longitudinal and transverse relaxation. **a,** The voltage profile during intermittent charging at 100 mA of 20 cm^3 of 100 mM DHAQ against 40 cm^3 of 200 mM K$_4$Fe(CN)$_6$. The red arrows indicate the times when the flow and electrochemical cycling were paused, and the relaxation measurements commenced. After the measurements finished, the flow and electrochemical cycling were resumed. **b,** T$_1$ and T$_2$ relaxation times of the HOD signal as a function of SOC. **c,** T$_1$ relaxation time of the DHAQ proton **b/b"** signal as a function of SOC. The error bars represent the 95% confidence level from the fit. **d,e,** Proton NMR spectra of DHAQ (H^a, H^b and H^c) and HOD acquired at a different flow rates via *on-line* detection, respectively. **f, g,** Signal integral of HOD and DHAQ as a function of flow rate and residence time in the detection region of the NMR probe, respectively. **h,** The FWHM of the HOD and DHAQ signals as a function of flow rate and residence time, and the labelling of protons.